HHS Public Access

Author manuscript

Dev Cell. Author manuscript; available in PMC 2024 December 04.

Published in final edited form as:

Dev Cell. 2023 December 04; 58(23): 2666–2683.e9. doi:10.1016/j.devcel.2023.10.002.

The Anaphase-Promoting Complex controls a ubiquitination-phosphoprotein axis in chromatin during neurodevelopment

Leya Ledvin[1], **Brandon M. Gassaway**[2], **Jonathan Tawil**[1], **Olivia Urso**[1], **Donald Pizzo**[1], **Kaeli A. Welsh**[3,4], **Derek L. Bolhuis**[5], **Daniel Fisher**[6], **Azad Bonni**[7], **Steven P. Gygi**[2], **Nicholas G. Brown**[3,4], **Cole J. Ferguson**[1,8]

[1]Pathology Department, University of California San Diego, La Jolla, CA 92093, USA

[2]Department of Cell Biology, Harvard Medical School, Boston, MA 02115, USA

[3]Department of Pharmacology, University of North Carolina School of Medicine, Chapel Hill, NC 27599, USA

[4]Lineberger Comprehensive Cancer Center, University of North Carolina School of Medicine, Chapel Hill, NC 27599, USA

[5]Department of Biochemistry and Biophysics, University of North Carolina School of Medicine, Chapel Hill, NC 27599, USA

[6]Institute of Genetics, Montpelier, France

[7]Neuroscience Department, Washington University, St. Louis, MO, 63110, USA

[8]Lead contact

SUMMARY

Mutations in the degradative ubiquitin ligase Anaphase-Promoting Complex (APC) alter neurodevelopment by impairing proteasomal protein clearance, but our understanding of their molecular and cellular pathogenesis remains limited. Here we employ proteomic-based discovery of APC substrates in APC mutant mouse brain and human cell lines, and identify the Chromosome Passenger Complex (CPC), Topoisomerase 2a and Ki-67 as major chromatin factors targeted by the APC during neuronal differentiation. These substrates accumulate in phosphorylated form, suggesting they fail to be eliminated after mitosis during terminal differentiation. Accumulation of the CPC kinase Aurora B within constitutive heterochromatin

*Correspondence: cferguson@health.ucsd.edu.

AUTHOR CONTRIBUTIONS

L.L, O.U., A.B., N.G.B. and C.J.F. conceived of the project. L.L and C.J.F. wrote the manuscript. B.M.G. and S.P.G. performed TMT proteomics. L.L. and J.T. performed imaging experiments. O.U. performed cell culture experiments and L.L generated mutant cell lines. J.T. and L.L performed image analysis. J.T. and L.L performed biochemistry experiments. L.L. and O.U. carried out in vivo injections. K.A.W., D.L.B., and N.G.B. conducted in vitro assays. D.P. performed Immunohistochemistry. D.F. engineered Ki-67 mutant mice.

DECLARATION OF INTERESTS

The authors declare no competing interests.

and hyperphosphorylation of its target histone 3 is corrected in the mutant brain by pharmacologic Aurora B inhibition. Surprisingly, reduction of Ki-67 but not H3S10ph rescued the function of constitutive heterochromatin in APC mutant neurons. These results expand our understanding of how ubiquitin signaling regulates chromatin during neurodevelopment and identify potential therapeutic targets in APC-related disorders.

Graphical Abstract

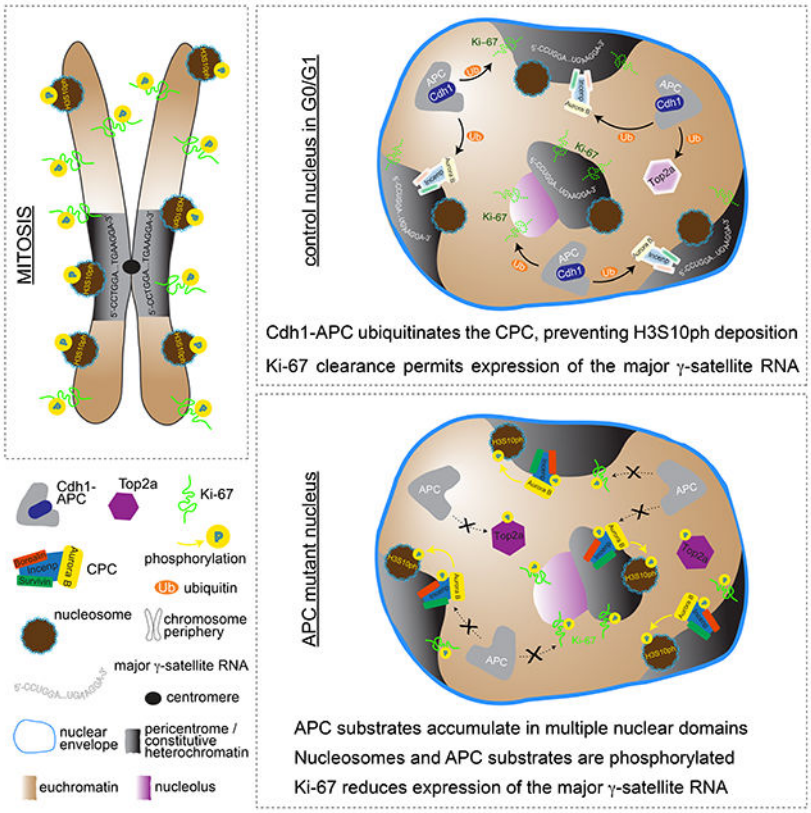

Keywords

Neurodevelopment; Ubiquitin ligase; Anaphase-Promoting Complex; Chromosome-Passenger Complex; H3S10ph; Ki-67; Topoisomerase; Chromatin; Heterochromatin; Proteomics/phosphoproteomics

INTRODUCTION

Turnover of macromolecules is fundamental to the development and function of all eukaryotic cells. In the nervous system, the multitude of diseases caused by protein accumulation underscores the essential role of degradative pathways in neuronal physiology. Ubiquitination, the covalent ligation of the small protein ubiquitin onto protein substrates, promotes degradation by the proteasome and represents the primary way cells eliminate specific proteins[1,2]. Ubiquitination requires sequential activity of E1 (ubiquitin-activating), E2 (ubiquitin-conjugating), and E3 (ubiquitin ligase) enzymes, with E3s largely governing

substrate selection[3]. Mutations in ubiquitin ligases alter neurodevelopment in humans, for instance *UBE3A* in Angelman syndrome, underscoring the importance of regulated proteolysis in neurons[4,5].

The 1.2 MDa ubiquitin ligase Anaphase-Promoting Complex (APC) represents a prototypical member of the RING class of E3s, which number >600 in humans[3]. Fourteen subunits of the mammalian APC are encoded by *ANAPC1–ANAPC8, ANAPC10–ANAPC13, ANAPC15* and *ANAPC16* (we represent human genes as *ANAPC7*, human proteins APC7, mouse genes *Anapc7* and mouse proteins Apc7). The subunits APC3, APC6, APC7, APC8 and APC12 homodimerize, and therefore 19 proteins constitute the core APC[6]. The APC regulates substrate degradation in diverse contexts, however until recently its contribution to inherited human disease was unknown[7,8]. We previously described the Ferguson-Bonni *ANAPC7* neurodevelopmental syndrome (OMIM 606949) in patients with loss of APC7[9]. Additional genes encoding APC subunits have also been linked to atypical neurodevelopment in patients[10,11]. Investigation of these disorders in model systems should elucidate fundamental mechanisms by which ubiquitin signaling drives neurodevelopment.

Ubiquitination by the APC proceeds in distinct stages[12,13]. Peptide motifs (e.g. destruction boxes, D-boxes) are recognized by the coactivators CDH1 (encoded by *FZR1*) or CDC20, which recruit substrates. The APC then initiates ubiquitination before ligating ubiquitin onto many substrate lysines. APC7 facilitates processive ubiquitination by stabilizing APC-substrate interactions[9]. Finally, the APC switches conformation to extend K11-linked ubiquitin chains recognized by the proteasome[12]. In general, CDC20 operates during mitosis, whereas the APC collaborates with CDH1 at every other stage, including in neurons[14].

Despite this molecular insight, how APC-substrate interactions contribute to health and drive disease remains largely unknown. A key finding from our exploration of Apc7 in mice was that Ki-67 is a neuronal APC substrate[9]. Localization of Ki-67 to constitutive heterochromatin established a neurodevelopmental role for the APC in this repressive compartment. Here, we use genetic, proteomic, imaging and biochemistry methods to expand the understanding of how the APC regulates chromatin factors within both heterochromatin and euchromatin, and go on to show how targeting APC substrates could be therapeutic in APC-related disorders of neurodevelopment. These findings broaden the role of ubiquitin signaling in neurodevelopmental chromatin regulation and identify potential routes toward rational treatment for inherited neurologic disease.

RESULTS

The Chromosome Passenger Complex (CPC) is a major APC target in neurons

To explore the neurodevelopmental functions of the APC, we examined APC-mediated protein clearance in the mammalian brain. We previously showed that Apc7-dependent phenotypes occur in differentiating neurons in the cortex, subcortical structures and the cerebellum, indicating that APC-mediated proteolysis is required across neuronal populations[9]. We focused our current proteomic evaluation on the cerebellum because the preponderance of granule neurons makes it comparatively homogenous[15]. Cerebellar

granule cells also proliferate and differentiate postnatally, greatly simplifying cell biological examination of neuronal differentiation in recessive mouse models[8,16,17]. To impair non-mitotic APC function in the brain, we generated Cdh1 mutant mice (*Fzr1*$^{f/f}$,Math1-cre) in which Cdh1 is deleted in most granule cell progenitors[18–20]. We also examined global Apc7 mutant mice homozygous for the patient-specific *Anapc7* null allele[9]. In both the Cdh1 and Apc7 mutants (collectively referred to as APC mutant mice), cerebellar histogenesis was unaffected[9]. In contrast, loss of mitotic APC function in granule cells of Cdc20 mutant mice (Cdc20$^{f/f}$,Math1-cre) caused cerebellar hypoplasia and malformation[9,19]. These mouse mutants establish in vivo systems for exploring the neurodevelopmental roles of the APC.

Because its substrates undergo proteasomal clearance, mutations that impact APC-mediated ubiquitination should specifically stabilize APC targets. Therefore, we performed unbiased quantitative mass spectrometry (MS)–based analysis of protein abundance in the cerebellar proteome of Cdh1 and Apc7 mutant mice. The use of Tandem Mass Tags (TMT) permits a multiplexed design that allows inclusion of 4 replicates of each mutant-control pair (Figure 1A)[21,22]. Granule neurons are generated in huge numbers from P5 to P7, therefore we chose P8 to maximize the representation of neurons undergoing the Cdh1-APC–dependent process of terminal differentiation. We detected 9452 unique proteins, of which 38 were elevated in the Cdh1 mutant and 21 were elevated in the Apc7 mutant (Figures 1B–1D, Table S1). The most dysregulated proteins in the Cdh1 mutant were members of the Chromosome-Passenger Complex (CPC), including the scaffold Incenp (inner centromeric protein), the kinase Aurora B, Survivin (Birc5) and Borealin (Cdca8) (Figures 1B and 1E). Importantly, the CPC was elevated in both mutants, although this phenotype was less severe in the Apc7 mutant, in agreement with previous proteomic experiments (Figure 1F)[9]. To determine whether CPC components were overexpressed, we performed reverse transcriptase quantitative PCR (RT-qPCR) analysis of Incenp and Aurora B mRNA. These transcripts were unaffected by Cdh1 loss (Figures 1G and 1H). Our results demonstrate that both Cdh1 and Apc7 drive clearance of the CPC in the brain, but Cdh1 plays the larger role. Hence, Apc7 loss is a hypomorph compared to the effects of Cdh1 loss.

Observing that the most dysregulated proteins were components of the CPC led us to explore its recognition and ubiquitination by the APC in vitro. As the scaffold and largest subunit of the CPC, INCENP directs its localization and activity[23,24]. Scaffolds typically bind to other subunits of a complex in precise stoichiometric ratios, which stabilizes the interacting proteins[25]. For these reasons, INCENP ubiquitination likely represents a critical step in the regulated clearance of the CPC. Despite its importance, APC-mediated recognition and ubiquitination of INCENP has not been systematically explored[26]. To gain insight into INCENP ubiquitination, we performed a series of in vitro assays using recombinant human APC and CDH1 along with the E1, E2s and ubiquitin[27]. The APC coactivator CDH1 recognizes substrates via D-box and/or KEN box motifs (Figure S1A)[28]. INCENP lacks KEN boxes but possesses four closely spaced D-boxes with the consensus RXXL sequence near the junction between an extended disordered region and a long alpha helix, according to structural predictions by AlphaFold (Figure S1B)[29]. Each D-box is conserved in the mouse (Figures S1C and S1D). We recombinantly expressed, purified, and fluorescently labeled the INCENP fragment corresponding to amino acids 256-632, which includes the D-boxes and much of the upstream disordered region (Figure S1E).

This INCENP fragment was avidly ubiquitinated by CDH1-APC in the presence of the E2 UBCH10/UBE2C (Figure S1F). Inclusion of the E2 UBE2S, which extends K11-linked ubiquitin chains, enhanced the generation of highly ubiquitinated INCENP products (Figure S1G). Compared to other APC substrates, INCENP was ubiquitinated more rapidly than the KEN box-containing N-terminus of KI-67, but less rapidly than the N-terminal 95 amino acids of CYCLIN B1 (Figure S1H). Truncation of the INCENP fragment to eliminate D-boxes 3 and 4 reduced the generation of highly ubiquitinated species by CDH1-APC (Figure S1I). Surprisingly, subsequent deletion of D-boxes 1 and 2 reduced but did not abolish ubiquitination (Figure S1I). These results provide a mechanism by which APC recognizes and ubiquitinates INCENP using canonical D-boxes and additional features within the disordered region.

The APC targets additional chromatin-associated proteins during neurodevelopment

Following proteomic identification of the CPC, we considered chromatin dysregulation as a pathogenic mechanism in APC-related neurodevelopmental disorders. The observation that the chromatin regulatory factors Ki-67 and Topoisomerase 2a (Top2a) were also elevated provided additional support for investigating chromatin in the APC mutant brain (Figure 1B). As the major Apc7-dependent substrate, Ki-67 was unique among APC substrates for its comparable accumulation in the brain of Apc7 and Cdh1 mutants (Figure 1F)[9]. We chose to focus on Top2a, an enzyme which relieves supercoils and thereby controls the topologic state of DNA, because it represents a functionally distinct chromatin factor that is regulated by Cdh1 but not Apc7 (Figure 1C). Loss of Cdh1 also caused elevation of cytoskeletal proteins related to the mitotic spindle, whereas Apc7 loss affected a more functionally diverse set of proteins (Figure 1D). Just 3 proteins were reduced in the Cdh1 mutant, in agreement with a primarily degradative role for the APC (Figure 1C).

During cerebellar development, granule cells undergo a stereotyped process of proliferation within the external granular layer (EGL) before they exit the cell cycle, migrate through the molecular layer (ML) and terminally differentiate (Figure 1I)[30]. During migration, axons of granule neurons form synapses with their primary target Purkinje neurons. After arriving in the internal granule layer (IGL), granule neurons become stably integrated into circuits[31]. Generation of most granule neurons occurs from ~P4 to P16, after which the EGL disappears[15]. To explore the tissue distribution of dysregulated chromatin factors, we performed detection by immunohistochemistry (IHC). In the control cerebellum, Aurora B-positive cells were restricted to the EGL (Figures 1J and 1K). However, in the Cdh1 mutant, positive cells were increased in the EGL and the IGL (Figures 1J and 1K). In the Apc7 mutant, Aurora B accumulation was confined to the EGL (Figure 1L). IHC detection of Ki-67 and Top2a demonstrated accumulation of each protein in both IGL and EGL of the Cdh1 mutant (Figures 1M–1O). Importantly, the abundance of other Topoisomerases was unaltered in the cerebellum APC mutants and RT-qPCR analysis in the Cdh1 mutant cerebellum showed no effect on *Top2a* expression (Figures 1P and 1Q). Immunoblots of APC substrates at P5, P13, and P26 confirmed these proteins are elevated in early cerebellar development (Figures 1R, 1S). Collectively, these observations indicate that APC-mediated ubiquitination controls degradation of multiple chromatin factors in developing neurons.

The CPC and Ki-67 accumulate in constitutive heterochromatin in APC mutant neurons

To examine the cellular localization of the CPC, we performed immunofluorescence detection of Aurora B in neurons. When isolated from P6 mice and subjected to primary culture ex vivo, cerebellar granule neurons (CGN) undergo similar developmental and morphogenic processes as those that occur in the brain[32]. To characterize the neurodevelopmental dynamics of Aurora B degradation, we examined CGN at the immature (DIV2, day 2 in vitro) and mature (DIV4) stages (Figure 2A). Aurora B localized to nuclei, as labeled by Hoechst (bisbenzimide). The fluorescence intensity of Aurora B in Cdh1 mutant nuclei was elevated at DIV2 and, to a lesser extent, at DIV4 (Figure 2B). Similar analyses in Apc7 mutant CGN showed a significant but less severe effect on Aurora B at DIV2 (Figures 2C and 2D). As an independent method of examining the subcellular distribution of APC substrates, we carried out immunoblot analysis of fractions isolated from the cerebellum at P11 (Figure 2E). Both Ki-67 and the CPC were enriched in chromatin, and their abundance was increased by loss of Cdh1 and Apc7 (Figures 2E and 2F). Importantly, Ki-67 and the CPC were not elevated in chromatin from the Cdc20 mutant cerebellum, indicating that mitosis-associated APC function is dispensable for clearance of these substrates (Figure 2G). These findings demonstrate that the CPC and Ki-67 accumulate within chromatin when APC function is impaired in neurons.

CPC localization is highly dynamic in cycling cells, whereas the localization of the CPC within neurons is unknown[23]. In APC mutant neurons, Aurora B overlapped with chromocenters, intensively Hoechst-positive structures in nuclei of mouse cells (Figures 2A and 2C). Chromocenters harbor compact, gene-poor pericentromeric DNA that corresponds to constitutive heterochromatin[33]. Relative to other neurons, constitutive heterochromatin is abundant in CGN, making these cells ideal for studying this compartment[34]. To assess the degree to which Aurora B and Hoechst were correlated subcellularly, we computed the Pearson R value for these signals within individual nuclei. Correlation between Aurora B and Hoechst increased significantly in APC mutant neurons (Figures 2H and 2I). To measure Aurora B intensity within chromocenters, we isolated regions of interest in the Hoechst channel through image processing steps before examining Aurora B fluorescence within them (Figure 2J). Aurora B was increased within chromocenters of both Cdh1 and Apc7 mutant neurons (Figures 2K and 2L). As an independent test of the spatial distribution of Aurora B, we performed immunofluorescence colabeling of Aurora B and H3K9me3, a histone modification associated with constitutive heterochromatin (Figure 2M). Subcellular correlation between Aurora B and H3K9me3 also increased in Cdh1 mutant nuclei (Figure 2N). In contrast, correlation between Aurora B and H3K27me3 was unaffected by Cdh1 loss, indicating Aurora B does not accumulate within H3K27me3-positive facultative heterochromatin (Figures S2A and S2B). Finally, we analyzed Aurora B in relationship to Ki-67, an APC substrate that also accumulates in constitutive heterochromatin, as indicated by its colocalization with H3K9me3 but not H3K27me3 in Cdh1 and Apc7 mutant neurons (Figures S2C–S2H). Immunofluorescence colabeling of Aurora B and Ki-67 demonstrated that these proteins accumulate in concert following loss of Cdh1 or Apc7 (Figures 2O–2Q). Subcellular examination of APC mutant CGN demonstrated an increase in the Pearson R value between Ki-67 and Aurora B, indicating these proteins accumulate in an overlapping

distribution (Figures 2R and 2S). These results establish that both the CPC and Ki-67 accumulate in constitutive heterochromatin of APC mutant neurons.

After observing that APC-dependent substrates accumulated in constitutive heterochromatin, we assessed the function of this compartment by performing RT-qPCR detection of RNA transcribed from the major γ-satellite found in pericentromeres. These AT-rich repetitive sequences represent a major component of constitutive heterochromatin in mouse cells, and the corresponding noncoding RNAs contribute to genome stability and heterochromatin formation[35]. The abundance of the major γ-satellite RNA declined over cerebellar maturation, compatible with a neurodevelopmental role (Figure 2T). Expression of the major γ-satellite was reduced in the developing Cdh1 mutant cerebellum, indicating that APC-mediated ubiquitin signaling controls the function of constitutive heterochromatin (Figure 2U).

We previously reported that loss of Apc7 also reduced the abundance of the major γ-satellite RNA in the developing cerebellum[9]. Because the magnitude of this deficit is similar between Cdh1 and Apc7 mutants, we hypothesized it could stem from Ki-67, which accumulates to similar degrees in each mutant. Therefore, to determine whether Ki-67 played a mechanistic role impairing major γ-satellite expression, we employed mice harboring an early frameshift mutation in *Mki67* (*Mki67*^{2ntΔ} allele) that reduces the abundance of Ki-67[36]. Because Ki-67 is the main Apc7-dependent substrate, whereas Cdh1 loss affects several other proteins to greater degrees, we crossed *Mki67*$^{2ntΔ/2ntΔ}$ mice with Apc7 mutant mice to minimize potential confounds. Homozygous mutation of *Mki67* resulted in similar amounts of Ki-67 in the cerebellum of both *Anapc7*$^{+/−}$,*Mki67*$^{2ntΔ/2ntΔ}$ and double mutant *Anapc7*$^{−/−}$,*Mki67*$^{2ntΔ/2ntΔ}$ mice (Figure 2V). RT-qPCR detection of the major γ-satellite RNA showed that depletion of Ki-67 was sufficient to restore its abundance in the Apc7 mutant cerebellum (Figures 2W). These results indicate that the APC regulates the function of constitutive heterochromatin in the brain through Ki-67.

Similar chromatin factors accumulate in G1-synchronized APC mutant RPE1 cells

Having identified roles for APC-mediated ubiquitination in neuronal chromatin, we wondered whether similar molecular interactions occur in other cellular contexts. Human RPE1 cells derived from the retinal pigment epithelium are a non-transformed, genetically stable near diploid cell line commonly employed to study chromatin because their large nuclei facilitate microscopy. To generate RPE1 cells with inactivating CDH1 mutations, we transduced guide RNAs (gRNAs) targeting different exons of *FZR1* into cells harboring doxycycline-inducible Cas9. After doxycycline treatment, we isolated clones derived from single colonies and sequenced the targeted exons to confirm the presence of biallelic frameshift mutations[37]. Control cells were treated identically except for Cas9 induction. RT-qPCR and RNA-seq confirmed reduction in the CDH1 transcript in mutant lines (Figures 3A and 3B). To determine how CDH1 controls protein degradation in RPE1 cells, we synchronized cells in G1 using the CDK 4/6 inhibitor Palbociclib before performing TMT-MS proteomic analysis of cell lysates[38]. In two lines of CDH1 mutant cells, we observed elevation of the CPC, KI-67 and TOP2A (Figure 3C, Table S3). Immunoblot analysis confirmed elevation of the CPC and H3S10ph (histone 3 phosphorylated at Ser10), a histone

modification deposited Aurora B (Figures 3D and 3E)[39]. Observing that similar proteins become elevated in CDH1 mutant RPE1 cells as in the Cdh1 mutant cerebellum links APC activity during G1 in cycling cells to G0 in developing neurons.

We performed immunofluorescence analysis of in RPE1 cells to explore the CPC in relation to other APC substrates. Whereas we were previously unable to detect Incenp in mouse neurons, we could readily detect human INCENP in RPE1 cells. We observed an increase in the intensity of INCENP, AURORA B and the CPC product H3S10ph in CDH1 mutant cells (Figures 3F–3J). The subcellular correlation between INCENP and H3S10ph also increased when CDH1 was mutated (Figure 3K). These results indicate that the CPC accumulates and is enzymatically active in CDH1 mutant RPE1 cells.

Whereas mouse cells contain chromocenters that represent constitutive heterochromatin, human cells do not possess discrete heterochromatic bodies. Therefore, we performed immunofluorescence colabeling of the CPC with H3K9me3. Both INCENP and AURORA B became highly correlated with H3K9me3 when CDH1 was lost, indicating that the CPC accumulates within constitutive heterochromatin when APC-mediated ubiquitination is impaired during G1 (Figures 3L–3O).

After TMT-MS demonstrated that TOP2A ranked among the most highly dysregulated proteins in CDH1 mutant RPE1 cells, we performed antibody-based detection of endogenous TOP2A (Figure 2C). Loss of CDH1 caused TOP2A accumulation in immunoblot and immunofluorescence analyses (Figures 3P–3R). However, in comparison to the CPC, TOP2A was more uniformly distributed throughout the nucleus (Figure 3Q). In agreement, TOP2A and AURORA B were correlated at the cellular level but not the subcellular level in CDH1 mutant RPE1 cells (Figures 3R and 3S). Immunofluorescence analysis in Cdh1 mutant CGN demonstrated that Top2a accumulation was significant and prolonged, failing to decline during neuronal maturation in the manner of Aurora B and Ki-67 (Figures S3A and S3B). Top2a in nuclei of Cdh1 mutant CGN was also more evenly distributed compared to Aurora B and Ki-67 (Figures S3A and S3D). Nevertheless, on a cellular basis, the intensity of Top2a in neuronal nuclei remained highly correlated with both Aurora B and Ki-67 (Figures S3C and S3E). These results indicate that APC-mediated ubiquitin signaling and substrate degradation are coordinated across nuclear domains.

KI-67 accumulates within nucleoli and constitutive heterochromatin in APC mutant RPE1 cells

During interphase in cycling cells, KI-67 localizes primarily to nucleoli, which typically reside in close association with constitutive heterochromatin[40–42]. Therefore, we examined KI-67 in RPE1 cells to determine if APC dysfunction altered its localization. Because APC7 promotes KI-67 degradation, we generated APC7 mutant RPE1 cell lines before isolating 2 mutant clones with APC7 loss (Figure 4A). Immunofluorescence analysis of G1-synchronized RPE1 cells demonstrated that loss of APC7 and CDH1 increased KI-67 (Figures 4B–4E). KI-67 localized to NUCELOLIN-positive nucleoli in both control and APC mutant RPE1 cells (Figures 4B, 4D, 4F and 4G). However, examination of KI-67 alongside H3K9me3 showed an increase in their subcellular correlation in APC mutant

RPE1 cells (Figures 4H–4K). These observations indicate that APC7 and CDH1 act during G1 to prevent KI-67 accumulation within both nucleoli and constitutive heterochromatin.

To investigate the spatial relationship between KI-67 and other APC substrates in RPE1 cells, we performed additional immunofluorescence colabeling experiments. Endogenous KI-67 and INCENP were correlated on a cellular basis in CDH1 mutant RPE1 cells (Figures 4L and 4P). We made similar observations when comparing KI-67 to AURORA B (Figures 4N and 4Q). At the subcellular level, KI-67 and CPC subunits were uncorrelated in control nuclei, however CDH1 loss caused these components to become modestly correlated (Figures 4M and 4O–4Q). Correlation between KI-67 and the CPC product H3S10ph also increased at the cellular and subcellular levels following CDH1 loss (Figures 4R–4T). These results indicate that APC dysfunction during G1 causes KI-67 accumulation in association with the CPC.

Finally, we explored the relationship between KI-67 and TOP2A at the cellular and subcellular levels using immunofluorescence (Figure 4U). Because they reside in non-overlapping nuclear territories, these APC substrates were completely uncorrelated subcellularly in control and CDH1 mutant RPE1 cells (Figure 4V). Nevertheless, the abundance of TOP2A and KI-67 remained highly correlated at the cellular level (Figure 4W). These observations indicate that APC-mediated ubiquitin signaling is required for the clearance of chromatin factors from different nuclear zones.

APC substrates accumulate as phosphoproteins in mutant neurons and RPE1 cells

TOP2A, KI-67 and the CPC play well-established roles in mitosis, a period when many chromatin-associated proteins are highly phosphorylated[43,44]. Therefore, we ascertained whether substrates accumulate in phosphorylated form in the APC mutant cerebellum by enriching phosphopeptides and performing TMT-MS–based phosphoproteomic analysis (Figure 5A). We detected 5610 unique phosphorylation sites on 2280 proteins (Table S2). Intriguingly, the most dysregulated phosphorylation site in the Cdh1 mutant was Ser1388 of Top2a (Figure 5B). Two additional phosphorylation sites on Top2a were also elevated by Cdh1 loss (Figure 5C). After ranking the scaled abundance of all phosphoproteins, Top2a-S1388ph went from below the 1st percentile in the control to become the top phosphoprotein in the Cdh1 mutant (Figure 5D). Phosphorylated Top2a was elevated to a lesser degree in the Apc7 mutant (Figure 5D). The scaled abundance of phosphorylated Incenp also rose to become ranked among the top 1% of phosphoproteins in the Cdh1 mutant (Figures 5E and 5F). Phosphorylated Ki-67 also increased in the cerebellum of Cdh1 and Apc7 mutants (Figures 5G and 5H). To examine the stoichiometry of phosphorylation, we compared the abundance of each phosphorylation site to the underlying protein, plotting the fold-change (mutant/control) in total protein abundance on the independent axis with the dependent axis showing fold-change (mutant/control) of each phosphorylation site. Because APC substrates lay near the line of slope 1, Top2a, Incenp and Ki-67 were phosphorylated in proportion to their abundance in the Cdh1 mutant (Figures 5I and 5J). These plots are compatible with a model in which phosphorylated APC substrates accumulate following Cdh1 loss mainly because of an increase in the abundance of the underlying proteins. These data

establish that APC substrates are phosphorylated and rise to become the most dysregulated phosphoproteins in the APC mutant brain.

As an independent test of the effects of APC dysfunction on the phosphoproteome, we performed TMT-MS–based phosphoproteomic analysis of G1-synchronized CDH1 mutant RPE1 cells. We detected 12,159 phosphorylation sites in 3510 proteins (Table S3). Several phosphorylation sites in INCENP and TOP2A were previously identified during phosphoproteomic analysis of mitotic cells[45]. Similar to the Cdh1 mutant brain, phosphorylated TOP2A, INCENP and KI-67 experienced major changes in scaled abundance and percentile rank upon CDH1 loss in RPE1 cells (Figure 5K). These results establish that substrates accumulate with a mitosis-associated phosphorylation pattern in APC mutant RPE1 cells.

A major mitosis-associated kinase, AURORA B has been investigated as a potential target in cancer, leading to the development of small-molecule AURORA B inhibitors[46–48]. These drugs had limited success in clinical trials, but they were relatively well-tolerated, raising the possibility that they could be administered during development[49–51]. To test whether phosphorylation of APC substrates resulted from AURORA B overabundance, we performed phosphoproteomic analysis of CDH1 mutant RPE1 cells under baseline conditions versus treated with the AURORA B inhibitor Barasertib. Immunoblots demonstrated that Barasertib rescued H3S10ph accumulation in CDH1 mutant RPE1 cells, demonstrating that this phenotype requires AURORA B activity (Figure 5L). Despite achieving pharmacologic AURORA B inhibition, we detected no change in the scaled abundance of any phosphorylated APC substrate in CDH1 mutant RPE1 cells (Figures 5M and S4H, Table S3). Similarly, in Cdh1 mutant cultured CGN, phosphorylated Top2a, Incenp and Ki-67 were unaffected by Aurora B inhibition (Figures 5N and S4I, Table S4). Accumulation of the phosphoprotein Tpx2, a mitotic microtubule nucleation factor, in mutant RPE1 cells and CGN was also independent of Aurora B activity (Figures S4A–S4F). These results indicate that phosphorylation of APC substrates does not require Aurora B activity. The observation that APC substrates are phosphorylated supports a model in which these proteins fail to undergo degradation in APC mutant neurons once progenitors exit mitosis and enter G0.

APC dysfunction in neurons causes hyperphosphorylation of histone 3

After determining that APC substrates were phosphorylated, we wondered whether additional phosphoproteins were regulated by the APC during neurodevelopment. A major Aurora B substrate in chromatin is the unstructured N-terminus of histone 3, which can be phosphorylated at Ser10 and Ser28 to generate H3S10ph and H3S28ph, respectively (Figure 6A)[52]. We hypothesized that Aurora B accumulation would alter histone phosphorylation in neurons and therefore performed IHC detection of H3S10ph and H3S28ph in the developing APC mutant cerebellum. The IGL of the Cdh1 mutant cerebellum showed increased H3S10ph positivity (Figure 6B). H3S10ph was also elevated in the EGL of Cdh1 and Apc7 mutants (Figure 6C). Surprisingly, H3S28ph was unaffected in the Cdh1 mutant (Figure 6D). Immunofluorescence analysis demonstrated H3S10ph accumulation in nuclei of both Cdh1 and Apc7 mutant CGN, but with distinct patterns. (Figure 6E). In Cdh1

mutant CGN, H3S10ph overlapped with H4K20me3-labeled constitutive heterochromatin, whereas H3S10ph in Apc7 mutant CGN formed small periheterochromatic foci (Figure 6E). In blinded analyses, we categorized the H3S10ph pattern as heterochromatic or periheterochromatic, both of which were rare in nuclei of control CGN (Figures 6F and 6G). Increased numbers of Cdh1 mutant CGN displayed the heterochromatic pattern of H3S10ph, whereas more Apc7 mutant CGN exhibited periheterochromatic H3S10ph (Figures 6F and 6G). Immunofluorescence colabeling experiments in Apc7 mutant CGN at DIV2 showed that H3S10ph was correlated with Ki-67 at the cellular level (Figures S5A–S5C). After setting a threshold for the intensity of Ki-67 and H3S10ph and tallying nuclei with >1 focus of saturating intensity for each protein, we found that the fraction of CGN harboring saturating Ki-67 and H3S10ph was increased by Apc7 loss (Figures S5D and S5E). H3S10ph saturation occurred almost exclusively in Apc7 mutant neurons that also contained saturating Ki-67 foci (Figure S5E). The effect of Apc7 on H3S10ph was specific to the post-mitotic period, as H3S10ph on the chromosome periphery was unaffected during mitosis in Apc7 mutant CGN on DIV2 (Figures S5F–S5H). These data support a model in which the APC controls histone phosphorylation in and around constitutive heterochromatin in post-mitotic neurons.

After demonstrating that APC mutation alters the composition and phosphorylation state within neuronal heterochromatin, we attempted to identify effects on other histone modifications associated with heterochromatin. Immunofluorescence analysis of CGN demonstrated that loss of Cdh1 or Apc7 had no effect on the abundance or distribution of histone modifications associated with constitutive or facultative heterochromatin (Figures 2M, S2A, S2B, S6A–S6F). Immunoblot analyses of the developing Apc7 mutant cerebellum also failed to show any effect on the abundance of histone modifications associated with constitutive heterochromatin (H3K9me3, H4K20me3, HP1a), facultative heterochromatin (H3K27me3) or euchromatin (H3K27ac) (Figure S6G). These results demonstrate that H3S10ph accumulation in neurons does not dramatically alter heterochromatin-associated histone modifications.

Aurora B inhibitors rescue H3S10ph accumulation in APC mutant neurons

If histone hyperphosphorylation in APC mutant neurons results from impaired clearance of Aurora B, then Aurora B inhibitors could reverse H3S10ph buildup and provide a mechanistic intervention in APC-related neurodevelopmental disorders. To determine whether Aurora B activity underlay H3S10ph accumulation in APC mutant CGN, we blocked Aurora B activity using Hesperadin, a selective Aurora B inhibitor that retains some activity toward Aurora A, and the newer agent Barasertib (AZD1152-HQPA) that is highly selective for Aurora B[50]. Application of these inhibitors to Cdh1 mutant CGN completely corrected H3S10ph accumulation (Figure 7A). Rescue occurred after just 60 minutes, suggesting that Aurora B continuously replenishes H3S10ph in APC mutant neurons. Loss of Cdh1 increased the area of H3S10ph signal saturation, and Aurora B inhibitors eliminated this phenotype (Figure 7B). Phenotypic correction of H3S10ph by Aurora B inhibitors was also observed in Apc7 mutant neurons (Figures S7A–S7E). These results establish that histone hyperphosphorylation in APC mutant neurons results from impaired clearance of the CPC and Aurora B.

To analyze the effect of Aurora B inhibition on H3S10ph within constitutive heterochromatin, we measured the subcellular correlation between H3S10ph and H4K20me3 in CGN. H3S10ph was highly correlated with H4K20me3 in constitutive heterochromatin in Cdh1 mutant CGN under baseline conditions (Figure 1C). Aurora B inhibition normalized the Pearson R value between H3S10ph and H4K20me3 in Cdh1 mutant CGN (Figure 1C). We observed similar effects in Cdh1 mutant neurons when comparing the subcellular correlation of H3S10ph and Hoechst-labeled chromocenters under baseline conditions versus Aurora B inhibition (Figure 7D). Application of Aurora B inhibitors also reduced the correlation between H3S10ph and H4K20me3 in Apc7 mutant neurons (Figure S7F). Measuring H3S10ph specifically within foci of constitutive heterochromatin, as delimited by H4K20me3 immunofluorescence, demonstrated that Aurora B inhibitors rapidly correct Cdh1-dependent H3S10ph elevation (Figures 7E and 7F). These results indicate that impaired clearance of the CPC and Aurora B causes dysregulation of H3S10ph within constitutive heterochromatin of APC mutant neurons.

Because Hesperadin and Barasertib were previously shown to cross the blood-brain barrier, we tested the effect of administering Aurora B inhibitors directly to Cdh1 mutant mice[49–51]. Remarkably, subcutaneous administration of both Barasertib and Hesperadin during cerebellar development rapidly and completely rescued the accumulation of H3S10ph in the Cdh1 mutant brain (Figure 7G). Despite correcting H3S10ph, serial administration of Barasertib during cerebellar development failed to increase the major γ-satellite RNA in the Cdh1 mutant cerebellum (Figure 7H). These observations indicate that Aurora B inhibitors can partially correct chromatin dysregulation in vivo in the developing mammalian brain (Figure 7I).

DISCUSSION

Chromatin dysregulation represents a major etiology in inherited neurodevelopmental disorders[53]. The identification of a mechanism by which ubiquitin-mediated proteolysis regulates the composition and phosphorylation state of chromatin underscores the importance of degradative pathways in the neuronal nucleus. APC mutation stabilizes the CPC in neurons, leading H3S10ph to accumulate. Because modification of the N-terminus of histone 3 is critical for epigenetic regulation, H3S10ph overabundance could interfere with chromatin interactions and perturb key mechanisms of cell-intrinsic differentiation[54,55]. Surprisingly, Aurora B inhibition did not rescue the major γ-satellite RNA, indicating that H3S10ph regulates other functions of heterochromatin.

Our observation that Top2a is controlled by Cdh1-APC provides evidence that DNA topology is under the regulation by APC-mediated ubiquitin signaling. Unlike Ki-67 and the CPC, Top2a localizes to euchromatin and stays elevated following maturation in APC mutant neurons. Hence, Top2a could play an outsized role in disease pathogenesis. Further examination of how APC substrates enzymatically modify chromatin should illuminate fundamental mechanisms of neurodevelopment.

An important attribute that distinguishes heterochromatin from euchromatin is its greater degree of compaction[56]. Constitutive heterochromatin behaves as a biomolecular condensate

formed by liquid-liquid phase separation, a physicochemical process that organizes chromatin domains through multivalent interactions between disordered macromolecules[57]. Several observations suggest that the APC could influence this process. First, ubiquitination affects phase separation of tagged proteins[58,59]. Second, the unstructured domain of INCENP drives phase separation of the neuronal APC substrate the CPC[60,61]. Third, the massive, surfactant-like Ki-67 could promote phase separation of heterochromatin per se or through its interaction with HP1a[62–65]. Fourth, the major γ-satellite RNA could also influence phase separation, as noncoding RNAs are enriched within nuclear condensates[66,67]. Finally, within membrane-free organelles, partitioning between the dilute and concentrated phases is heavily influenced by charge and phosphorylation state[68]. Histone 3 and APC substrates accumulate as phosphoproteins upon Cdh1 loss, indicating the mitotic state of phosphorylation carries over into neuronal nuclei. Perturbing the biophysical properties of chromatin could disrupt the distribution of chromatin-associated factors, with the potential for lasting effects on neurodevelopmental gene regulation.

Despite their prevalence, few therapies exist that alter the pathogenesis of inherited disorders of neurodevelopment, rendering this class of diseases a major unmet medical need[69,70]. Through a combination of unbiased and hypothesis-driven experiments, we identify multiple pathologic targets which could be manipulated therapeutically in APC-related disorders of neurodevelopment.

Limitations of the Study

While this study reports progress on the cellular and molecular underpinning of APC-related neurodevelopmental disorders, important knowledge gaps persist. For instance, why are distinct subsets of APC substrates stabilized by loss of Cdh1 versus Apc7, and what accounts for the difference in H3S10ph distribution in APC mutant neurons? How are CPC subunits recognized and ubiquitinated, and how does complex formation impact this process? While INCENP is an APC substrate in vitro, how INCENP is ubiquitinated in cells necessitates examination. Understanding how >30 other neuronal APC substrates contribute to disease pathogenesis will require subsequent experimentation. We do not know how H3S10ph controls heterochromatin or the chromosome periphery, or which specific processes are affected by H3S10ph accumulation in neurons. The consequences of perturbing the phosphoproteome during interphase must be experimentally tested to determine how phosphoproteins exert distinct effects relative to their unmodified counterparts. Characterizing the effects of the major γ-satellite noncoding RNA on heterochromatin formation under the regulation of the APC and Ki-67 necessitates additional study. Finally, to determine which specific neuronal processes are perturbed by APC mutation, and to dissect the effects of Ki-67 versus H3S10ph in these phenotypes, demands future inquiry.

STAR METHODS

RESOURCE AVAILABILITY

Lead contact: Further information and requests for resources and/or reagents should be directed to the Lead Contact, Cole Ferguson (cferguson@health.ucsd.edu).

Materials availability: All mouse lines, cell lines, purified proteins or any other non-commercially available reagent generated or used during this study will be made freely available to interested researchers.

Data and code availability:

- The TMT proteomics and phosphoproteomics datasets “Investigation of cerebellum-specific knockouts of Cdh1 and Apc7,” “Phosphoproteomic analysis of Aurora B inhibition in WT and CDH1 mutant RPE1 cells,” and “Investigating the effect of Aurora B inhibition in WT and Cdh1 mutant primary neuron cultures,” have been deposited at ProteomeXchange via the PRIDE database and are publicly available as of the date of publication. Accession numbers for these datasets are listed in the key resources table. Original/source data have been deposited on Mendeley Data and are publicly available as of the date of publication. DOIs are listed in the key resources table.
- This paper does not report original code.
- Any additional information required to reanalyze the data reported in this paper is available from the lead contact upon request.

EXPERIMENTAL MODEL AND STUDY PARTICIPANT DETAILS

Mice: Animals were cared for in accordance with NIH guidelines. All experimental methods were approved by the UCSD Institutional Committee on the Use and Care of Animals under the protocol number S20121. Animals were housed in a 12:12 light:dark cycle. In general, we employed trio breeding. Pups were genotyped at P4-P5 by tail biopsy and weaned into sex-matched cages at P21 to be bred at 7-8 weeks. Animals were allocated to experimental versus control groups based on genotype. Sex matched-littermate controls were used in all experiments, and the age at which animals were used is reported in figure legends.

The *Anapc7* mutation was maintained on the hybrid C57BL/6 x 129 mixed background through cousin mating. These animals served as the source for primary granule neuronal cultures and all imaging experiments. The *Anapc7* mutant allele was also maintained on the congenic Jackson C57BL/6 background, which were used in proteomic experiments. For experiments with Apc7 mutant mice, $Anapc7^{+/-}$ mice served as controls when available, but $Anapc7^{+/+}$ were also used if heterozygotes were unavailable.

For crosses involving mice harboring floxed *Fzr1* and floxed *Cdc20*, as well as the Math1-cre mice, all mice were maintained on the congenic Jackson C57BL/6 background, having being backcrossed for more than 5 generations[19,71]. To generate experimental animals, mice homozygous for each floxed allele were crossed with mice heterozygous for the floxed allele and positive for Math1-cre. We brought in the Math1-cre from both the paternal and maternal sides to assess the possibility of germline inactivation of cre, which was not observed. Mice which were homozygous for the floxed allele and positive for Math1-cre were used as experimental animals, while sex-matched littermates that were floxed

heterozygotes and positive for Math1-cre were used preferentially as controls to account for potential cre-mediated effects, although other genotypes were allowed if necessary.

Double mutant mice for Apc7 and Ki-67 were generated in the following fashion. *Anapc7*$^{+/-}$ were crossed with *Mki67*$^{2ntΔ/2ntΔ}$ on the BL/6 background to generate double heterozygotes. These offspring were then intercrossed to generate male and female mice of the genotype *Anapc7*$^{+/-}$, *Mki67*$^{2ntΔ/2ntΔ}$ mice. *Anapc7*$^{+/-}$, *Mki67*$^{2ntΔ/2ntΔ}$ mice were then crossed to generate Apc7 wild-type and Apc7 mutant mice on the Ki-67 mutant background.

Human subjects: This study included no human subjects.

Cell lines: RPE1 (hTERT-RPE-1) cells expressing doxycycline-inducible Cas9 were previously described[72]. Cells were maintained in DMEM/F-12 media supplemented with 10% fetal bovine serum plus antibiotics and grown at 37 degrees in 5% CO2. Cells were split 1:10 every 3-4 days.

METHOD DETAILS

Mouse Proteomic and Phosphoproteomic Sample Processing—Frozen mouse cerebella were processed using the streamlined TMT labelling protocol in a similar fashion as previously adapted for mouse cerebella[9,21]. Processing included lysis with 8M urea in 200 mM EPPS pH 8.5 with protease and phosphatase inhibitors, reduction with 5 mM TCEP, alkylation with 10 mM iodoacetamide, and quenching with 5 mM DTT. This was followed by methanol/chloroform precipitation of 100 μg of protein, reconstitution in 200 mM EPPS pH 8.5, digestion overnight at room temperature with 1:100 LysC and digestion with 1:100 trypsin at 37°C. Peptides were labelled by adding anhydrous acetonitrile to ~30%, followed by labelling with TMT16 reagent. 1% of each labeled sample was combined and analyzed unfractionated to ensure labeling efficiency was >97% and that the samples are mixed at a 1:1 (total amount) ratio across all conditions. After mixing, labelled peptide samples were de-salted using a 200 mg Sep-Pak cartridge, followed by drying in a rotary evaporator. Phosphopeptides were enriched using a Fe-NTA spin column and desalted via StageTip for LC-MS/MS analysis, while the flow-through was dried, reconstituted in 5% ACN 10 mM ammonium bicarbonate, and fractionated using basic pH reverse phase chromatography on an Agilent 300extend-C18 column (3.5 μm, 4.6x250 mm) using an Agilent Infinity 1260 HPLC. Peptides were subjected to a 75 min linear gradient from 13% to 42% of Buffer B (10 mM ammonium bicarbonate, 90% ACN, pH 8) at a flow rate of 0.6 mL/min, resulting in a total of 96 fractions which were consolidated into 24 by combining (in a chessboard pattern) four alternating wells down columns of the 96-well plate. Each combined fraction was desalted via StageTip for SPS-MS3 analysis.

RPE1 Proteomic and Phosphoproteomic Sample Processing of RPE1 and Primary Cerebellar Neuron Cultures—For RPE1 cells, cell cultures were harvested by washing 1x with PBS, scraping cells into 1 mL of PBS, pelleting cells by centrifugation, removal of supernatant, and freezing in liquid nitrogen. Frozen cell pellets were lysed in 8 M Urea in 200 mM EPPS pH 8.5 with protease and phosphatase inhibitors.

Primary cerebellar granule neurons were harvested by washing 1x with PBS, then adding lysis buffer (8 M Urea in 200 mM EPPS pH 8.5 with protease and phosphatase inhibitors), followed by freezing in liquid nitrogen.

RPE1 and primary neuron cell lysates were processed using the streamlined TMT protocol as previously described[21]. Processing included lysis with 8 M urea in 200 mM EPPS pH 8.5 with protease and phosphatase inhibitors, reduction with 5 mM TCEP, alkylation with 10 mM iodoacetamide, and quenching with 5 mM DTT. This was followed by methanol/chloroform precipitation of 100 μg of protein, reconstitution in 200 mM EPPS pH 8.5, digestion overnight at room temperature with 1:100 LysC, and digestion with 1:100 trypsin at 37°C. Peptides were labelled by adding anhydrous acetonitrile to ~30%, followed by labelling with TMTpro reagent. 1% of each labeled sample was combined and analyzed unfractionated to ensure labeling efficiency was >97% and that the samples are mixed at a 1:1 (total amount) ratio across all conditions. After mixing, labelled peptide samples were de-salted using a 200 mg Sep-Pak cartridge followed by drying in a rotary evaporator. Phosphopeptides were enriched using a Fe-NTA spin column and desalted via StageTip for HCD hrMS2 analysis, while the flow-through was dried, reconstituted in 5% ACN 10mM ammonium bicarbonate, and fractionated using basic pH reverse phase chromatography on an Agilent 300extend-C18 column (3.5 μm, 4.6x250 mm) using an Agilent Infinity 1260 HPLC. Peptides were subjected to a 75 min linear gradient from 13% to 42% of Buffer B (10 mM ammonium bicarbonate, 90% ACN, pH 8) at a flow rate of 0.6 mL/min, resulting in a total of 96 fractions which were consolidated into 24 by combining (in a chessboard pattern) four alternating wells down columns of the 96-well plate. Each combined fraction was desalted via StageTip for RTS-SPS-MS3 analysis.

Proteomic Data Collection—Mass spectra were collected on an Orbitrap Fusion Lumos mass spectrometer or Orbitrap Eclipse mass spectrometer (ThermoFisher Scientific) coupled to a nanoEASY-nLC 1200 LC pump (ThermoFisher Scientific). Peptides were separated on a 35 cm column (i.d. 100 μm, Accucore, 2.6 μm, 150 Å) packed in-house using a 90 min gradient (from 5% −30% acetonitrile with 0.1% formic acid) at 500 nl/min. Data were collected using a Real-time search (RTS) SPS-MS3 method[73–76]. MS1 data were collected using the Orbitrap (120,000 resolution; maximum injection time 50 ms; AGC 4e5, 400-1400 m/z). Determined charge states between 2 and 5 were required for sequencing and a 120s dynamic exclusion window was used. MS2 scans consisted of collision-induced dissociation (CID), quadrupole ion trap analysis, AGC 2E4, NCE 35, q-value 0.25, maximum injection time 35 ms, and isolation window of 0.7 Da using a Top10 method. Through Thermo Fisher Scientific's instrument application-programming interface (iAPI) for Tribrid mass spectrometers, an on-line real-time search algorithm (using the UniProt Mouse database, December 2018) was used to trigger MS3 scans for quantification[73,74]. MS3 scans were collected in the Orbitrap at a resolution of 50,000, NCE of 65%, maximum injection time of 100 ms, and AGC of 1.5e5.

Mouse Phosphoproteomic Data Collection—Mass spectra were collected on Orbitrap Fusion Lumos mass spectrometer (ThermoFisher Scientific) coupled to a nanoEASY-nLC 1200 LC pump (ThermoFisher Scientific). Peptides were separated on a

35 cm column (i.d. 100 μm, Accucore, 2.6 μm, 150 Å) packed in-house using a 180 min gradient (from 5% -30% acetonitrile with 0.1% formic acid) at 500 nl/min. Data was collected using a multi-notch SPS-MS3 method[75,76]. MS1 data were collected using the Orbitrap (120,000 resolution; maximum injection time 50 ms; AGC 4e5, 400-1400 m/z). Determined charge states between 2 and 5 were required for sequencing and a 120 second dynamic exclusion window was used. MS2 scans consisted of collision-induced dissociation with multi-stage activation (CID-MSA) or higher collision energy dissociation (HCD), quadrupole ion trap analysis, automatic gain control (AGC) 2E4, NCE (normalized collision energy) of 35, q-value 0.25, maximum injection time 35 ms, and isolation window of 0.7 Da using a Top10 method. MS3 scans were collected in the Orbitrap at a resolution of 50,000, NCE of 65%, maximum injection time of 250 ms, and AGC of 1.5e5.

RPE1 and Primary Cerebellar Neuron Phosphoproteomic Data Collection— Mass spectra were collected on Orbitrap Eclipse mass spectrometer (ThermoFisher Scientific) coupled to a nanoEASY-nLC 1200 LC pump (ThermoFisher Scientific). Peptides were separated on a 35 cm column (i.d. 100 μm, Accucore, 2.6 μm, 150 Å) packed in-house using a 180 min gradient (from 5% −30% acetonitrile with 0.1% formic acid) at 500 nl/min. Data was collected using a multi-notch SPS-MS3 method[75,76]. MS1 data were collected using the Orbitrap (120,000 resolution; maximum injection time 50 ms; AGC 4e5, 400-1400 m/z). Determined charge states between 2 and 5 were required for sequencing and a 120 second dynamic exclusion window was used. MS2 scans consisted of higher collision energy dissociation (HCD) followed by Orbitrap analysis, with a resolution of 50,000, automatic gain control (AGC) 1.5E5, NCE (normalized collision energy) of 36, q-value 0.25, maximum injection time 250 ms, and isolation window of 0.5 Da using a Top10 method.

Mass Spectrometry Data Processing—Mass spectra were processed using a SEQUEST-based software pipeline and subsequently analyzed on the Perseus platform[77–79]. Data were searched against the UniProt Mouse database (December 2018), using a 20-ppm precursor ion tolerance for total protein-level analysis and 0.9 Da product ion tolerance. TMT16 and carbamidomethylation of cysteine were set as static modifications, while methionine oxidation, asparagine/glutamine deamidaion, and serine/threonine/tyrosine phosphorylation (for phosphopeptide enriched runs) as variable modifications. Peptide-spectrum matches (PSMs) were identified, quantified, and filtered to a 1% peptide false discovery rate (FDR) and then collapsed further to a final protein-level FDR of 1%. Proteins were quantified by summing reporter ion counts across all matching PSMs. Briefly, a 0.003 Da (3 millidalton) window around the theoretical m/z of each reporter ion was scanned and the maximum intensity nearest the theoretical m/z was used. Phosphorylation sites were localized using AScorePro[80]. Reporter ion intensities were adjusted to correct for the isotopic impurities of the different TMT reagents according to manufacturer specifications and adjusted to normalize ratios across labelling channels. Lastly, for each protein, signal-to-noise (S:N) measurements of the peptides were summed and then normalized to 100.

The mass spectrometry proteomics data have been deposited to the ProteomeXchange Consortium via the PRIDE partner repository with the identifiers listed in the KRT[81].

Cloning—Fragments of the human INCENP coding sequence were ordered as synthetic DNA molecules from Twist Biosciences and cloned into pGEX vectors using BamHI and NotI sites. Fragments were designed to be expressed as N-terminal GST fusion proteins with an intervening TEV site and a C-terminal 6-His tag[82].

Protein purification and APC-dependent substrate ubiquitination assays—UBA1, ubiquitin, UBCH10, UBE2S, CDH1, Cyclin B (residues 1-95), and Ki-67 (residues 1-300) were purified as previously described[9,27]. A phosphomimetic version of the APC was used as the E3 ubiquitin ligase in the enzyme assays[83]. The human INCENP protein fragments were expressed as N-terminal, TEV-cleavable GST fusions and purified using glutathione Sepharose (GST) resin. After TEV-dependent proteolytic cleavage, the INCENP truncations were separated from free GST by nickel affinity chromatography and fluorescently labeled using sortase. In this step, a fluorescent LPETGG peptide was ligated to the N-terminus of the INCENP truncations during an overnight reaction kept on ice containing 1 μM sortase, 25-50 μM Incenp, 20x excess peptide, and sortase buffer (50 mM Tris pH 7.6, 150 mM NaCl, 10 mM $CaCl_2$). Fluorescently-labeled INCENP fragments were then purified using buffer exchange columns to remove excess peptide, followed by size exclusion chromatography.

For APC-dependent ubiquitination assays, reactions containing 100 nM UBA1, 250 nM E2, 30 nM APC, 150 nM CDH1, 100 μM of ubiquitin, 5 mM of Mg^{2+}/ATP, and 100 nM substrate were incubated at room temperature then quenched at the indicated time points. Reactions containing INCENP fragments with deleted D-boxes contained 200 nM of substrate. Substrate ubiquitination was monitored by fluorescent scanning of SDS-PAGE gels using an Amersham Typhoon.

Fractionation of mouse brain—Dissected cerebella were diced and subjected to 10 strokes with Dounce A in cold hypotonic buffer (20 mM HEPES pH 7.9, 1 mM $MgCl_2$ and 10 mM KCl) containing 1 mM DTT and protease and phosphatase inhibitor cocktails. Samples were rotated at 4 degrees for 15 min before 20 more strokes with Dounce A and filtration through a 40 um mesh. This was sampled as the total fraction before centrifugation at 500 x*g* for 5 min to isolate the nuclei and collect the supernatant representing the cytoplasmic fraction. Half the nuclear fraction was digested with benzonase to generate the benzonase-treated nuclear supernatant and chromatin pellet. The other half of the nuclear fraction was treated identically except for benzonase treatment. Triton X-100 was added to all samples at a final concentration of 0.2% before benzonase was added to the appropriate fractions and samples rotated at 4 degrees for 60 min. NaCl was then added to a final concentration of 300 mM to lyse nuclei. Samples were vortexed and rotated for 15 more minutes before centrifugation at >16,000 x*g* to collect insoluble chromatin, which was washed and resuspended in buffer to uniformity.

Protein quantitation in lysates—We used the Bradford reagent to quantify protein throughout this study. Each sample was assayed in triplicate and the median value taken. Complete lysis buffer served as the blank.

Immunoblotting—For immunoblots we used Invitrogen NuPage Bis-Tris 4%–12% gels and LDS sample buffer followed by transfer onto Nitrocellulose membranes via tank immersion. To quantitate loading, prior to blocking membranes were incubated with the ReVert total protein stain (LI-COR) and imaged on a LI-COR Odyssey CLx. This stain was then removed using the manufacturer's method. Blocking and antibody-incubation steps were performed in Tris-buffered saline with 0.1% Tween-20 and 3% BSA. Infrared fluorescent secondary antibodies were detected by the LI-COR Odyssey CLx. After adjusting brightness and contrast in the LI-COR software Blots were imaged at 300 dpi and we did not perform any further processing of raw images after the acquisition step. Exposure time was chosen to avoid pixel saturation.

Quantitative reverse transcriptase PCR (RT-qPCR)—Total RNA was isolated using Trizol and the column-based RNeasy kit. For assessing the abundance of transcripts for Incenp, Top2a and Aurora B, we generated cDNA using the iScript reagent. A no RT control was used for each amplicon to ensure there was not spurious amplification of contaminating DNA. The abundance of each transcript was normalized to GAPDH. Each amplicon was designed to be 100-250 nucleotides and to span an intron > 1 kb. We used the SYBR green reagent and the Bio-Rad CFX96 Real-Time System.

For assessment of expression of major γ-satellite noncoding RNA, we began by isolating RNA as described above. We then treated RNA with DNase I before generated cDNA using iScript. We included the essential no-RT control in our experiment and subtracted any residual signal reflecting contaminating DNA, which was usually negligible. The abundance of the major γ-satellite RNA was then normalized to GAPDH.

Bulk RNA-seq and Processing—RPE1 cell pellets were resuspended in Trizol. Total RNA was isolated using the column-based Qiagen RNeasy kit. Library prep was performed using Illumina Stranded Total RNA Prep Ligation with Ribo-Zero Plus (Illumina). The prepared libraries were subsequently sequencing using the NovaSeq S4 High-Output platform to generate 50 bp paired-end reads. Each sample was sequenced to a depth of at least 20 million reads. Sequenced reads were aligned to GRCh38.p14 human reference genome with the gencode-vH29 annotations using STAR Aligner version 2.7.9a. BAM files were indexed using samtools index and the resulting indexed BAM files were converted to BigWig files using bamCoverage.

Generation of inducible mutation in *FZR1* and *ANAPC7* using CRISPR-Cas9 in RPE1 cells—To generate inducible FZR1 knock-out RPE1 lines, we used a similar strategy as described before[72]. In brief, four gRNAs targeting FZR1 (see Table S1) originating from the Brunello gRNA library[37] were cloned into the lentiGuide-Puro vector. Lentiviral particles were generated by transfecting the constructs into HEK293T cells using Lenti-X Packaging Single Shots (Takara Bio). Virus-containing culture supernatant was collected at 48 hours and 72 hours. The supernatant was then concentrated using PEG-IT Virus Precipitation Solution before adding to RPE1 cells.

RPE1 cells expressing Cep192-mNeonGreen (*in situ*-tagged) and doxycycline-inducible Cas9 were infected with the gRNA lentiviruses in the presence of 8 mg/ml of polybrene

(EMD Millipore) and selected with 14 mg/ml of puromycin[72]. To induce Cas9 expression, cells were treated with 0.1 mg/ml of doxycycline for 24 hr. After washing doxycycline off, cells were incubated for 48 hr. Cells were then collected and their genomic DNA was extracted and amplified by PCR using GoTaq DNA Polymerase and specific oligo pairs for each gRNA (see Table S1). PCR products were analyzed by Sanger sequencing to assess the induction of indels upon Cas9 expression. The FZR1 transcript was assessed using RT-qPCR and RNAseq, whereas APC7 expression was assessed using IB. To isolate single cells, we performed a series of serial dilutions in 96 well plates. Wells were visually assessed to determine which wells were seeded with a single colony-forming unit.

RPE1 Synchronization—RPE1 cells were plated at 30% confluency. After 24 hours, cells were treated with 1 μM Palbociclib for 18 hours.

Cerebellar granule neuronal culture—Cultures of mouse primary cerebellar granule neurons were generated from P6-P7 mice as previously described[32]. For imaging experiments, primary granule neurons were plated onto acid treated, poly-L ornithine coated optical cover glass in 24 well dishes with 700,000 cells per well. For immunoblotting and TMT-MS experiments, neurons were plated onto PLO coated plastic 3.5 cm dishes with 4.5 million cells per well.

Immunocytochemistry—Cells grown on optical cover glass were fixed in 4% PFA for 15 minutes at room temperature for detection of most targets. In neurons, H4K20me3 and H3S10ph were detected following fixation with cold 1:1 methanol:acetone solution for 5 minutes at room temperature. Cells fixed with 1:1 Methanol:Acetone solution were allowed to air dry for 5 minutes prior to gentle rehydration with PBS. H3S10ph could be detected in RPE1 cells following PFA fixation. All fixed cells were washed twice with PBS solution after fixation. Permeabilization was performed using a solution 0.3% PBS-Triton for 30 minutes followed by blocking in 2% normal goat serum for 30 minutes. Primary antibodies were incubated overnight at 4 degrees. Cells were washed before applying fluorophore-labeled secondary antibodies and Hoechst for 1 hour at room temperature, then washed again and mounted.

Histology—Brains were immersion fixed overnight in neutral-buffered formalin at 4 degrees before processing for routine histology with H&E staining. Brightfield imaging was performed on an Olympus BX51 equipped with Olympus DP71 camera.

Confocal imaging—We primarily used the A1R system at the UCSD Nikon Imaging Center. Three color images were acquired in laser scanning confocal mode with the Resonant scanner. 0.25 μm Z-stacks were acquired over the entire of thickness of imaged cells. For displayed images, Z stacks were flattened by making maximum intensity Z-projections in ImageJ[84]. Each image contained an average of between ~25-60 cells. To ensure there was no bias in the choice of individual fields for imaging, each field was chosen based exclusively upon the Hoechst channel with the microscopist agnostic to the signal in other channels. In general, post-processing was performed in Photoshop only for images which were displayed, whereas raw images were used for quantitative analysis.

Image analysis – generating binaries and measuring total immunofluorescence intensity—Raw images of primary cerebellar granule neurons were acquired as described above and processed in the NIS Elements software. Maximum intensity Z projections were generated for every image. The Hoechst channel was used to define regions of interest (nuclei) and binaries were manually generated within these boundaries. During analysis of cultured neurons, apoptotic cells or cells that did not display cerebellar granule neuron morphology were manually excluded. The mean object intensity for indicated markers was then measured within these nuclei binaries.

Image analysis – subcellular correlation—After generating the binaries on nuclei, maximum intensity projections of confocal micrographs were analyzed using the Pearson R Colocalization feature in NIS Elements. This function computes the Pearson R value on a pixel-by-pixel basis within a region of interest, in this case a single nucleus.

Image Analysis – chromocenters—Difference of Gaussians was applied to the Hoechst signal in three-color images of primary granule neurons. Rolling Ball background subtraction was applied followed by bright spot detection to generate binaries containing areas of saturating Hoechst signal. These binaries were then dilated slightly to generate the final chromocenters. The signal from other detected proteins was measured within chromocenters.

Image Analysis – constitutive Heterochromatin—Three color images of primary granule neurons were acquired as described above. Maximum intensity projections of the raw confocal micrographs were generated. Two pre-processing steps, Rolling Ball and Smoothing, were applied to the channel containing the signal for H4K20me3. A threshold was set for the H4K20me3 signal to generate the binaries for constitutive heterochromatin. The mean intensity of Aurora B and H3S10ph was then measured within these binaries.

Image Analysis - H3S10ph Foci—Maximum intensity Z projections were generated of the raw confocal micrographs prior to applying two pre-processing steps: Rolling Ball and Smoothing. A threshold was set based on intensity of the H3S10ph signal. Object count and object areas for the H3S10ph or green channel were measured for each entire image. The number of saturating foci above threshold were manually counted for each nucleus. These areas were added to calculate the total area of saturating H3S10ph per nucleus.

Confocal imaging - mitosis—For imaging of mitotic cells, we used the Zeiss 880 LSM2 equipped with Airyscan hexagonal detector array at the UCSD Microscopy Core for near super-resolution confocal microscopy. Primary cultures of cerebellar granule neurons were fixed and subjected to immunostaining as described above at DIV2. We used the 63x objective combined with 7x digital zoom to acquire 0.16 μm optical sections prior to Airyscan post-processing with default settings. Post-processing was performed in Photoshop only for images which were displayed, whereas raw images were used for quantitation.

Image analysis – linear intensity—Cells at different stages of mitosis were identified based upon chromosomal morphology and imaged as described above before being analyzed in a blinded fashion. To assess the fraction of Ki-67 and H3S10ph on the chromosome

periphery, fluorescence intensity was measured in NIS-Elements along a line starting from the outside, representing 0 μm and bisecting the chromosome periphery perpendicularly. Two lines were drawn per image at opposite different points along rhe chromosome periphery. Fluorescence intensity values were then aligned based upon peak fluorescence.

Drug Treatment – cultured cells—In general, all small molecules were diluted in DMSO and introduced into the culture medium through half volume changes at a concentration that was twice the intended final concentration. A similar process with the same amount of DMSO but no drug was used in untreated wells. In this way there was carryover of conditioned media during treatment.

Drug Treatment – mice—Mice were weighed prior to injection. Stock solutions of Barasertib and Hesperadin in DMSO were diluted in PBS and injected subcutaneously on the flank. Untreated mice underwent sham injections containing equivalent amounts of DMSO but no drug. Tissue was collected 4 hours post-injection and fixed in formalin for immunohistochemistry.

Immunohistochemistry—Tissue sections were cut from blocks of formalin-fixed paraffin embedded mouse brains at age P10. 5 μm tissue sections were stained with antibodies to Aurora B (1:300), Ki-67 (1:12,000), Top2a (1:1500), H3S10ph (1:75) and H3S28ph (1:300). Slides were stained on a Ventana Discovery Ultra (Ventana Medical Systems, Tucson, AZ, USA). Antigen retrieval was optimized for each epitope individually and was performed using CC1 (Tris-EDTA based; pH 8.6) for 40 (Ki-67, Aurora B, Top2a) or 92 minutes (H3S10ph, and H3S28ph) at 95 degrees. The longer retrieval for H3S10ph antibodies was determined to be critical for full detection of the relatively low-expressing epitope. The primary antibodies were incubated on the sections for 32 minutes at 37 degrees. For Ki-67 (a rat primary) sections were incubated with a rabbit anti-Rat antibody (1:3000). Primary (or secondary) antibodies were detected with an HRP polymer-linked anti-Rabbit (OmniMap, Ventana Medical systems). Antibody presence was visualized used DAB as a chromagen followed by hematoxylin as a counterstain. Slides were rinsed, dehydrated through alcohol and xylene and coverslipped.

QUANTIFICATION AND STATISTICAL ANALYSIS

We used GraphPad Prism 10 software to perform the statistical tests described in figure legends. In general, for parametric data with two comparators, we used the two-tailed student’s t-test. For nonparametric data with two comparators, we used the Kolmogorov-Smirnov test. The Kruskal-Wallis test was used for comparisons of non-parametric data between three or more groups followed by Dunn test. For details of the quantitative methods used in TMT proteomics, please refer to the above sections.

Supplementary Material

Refer to Web version on PubMed Central for supplementary material.

ACKNOWLEDGMENTS

We thank members of the Ferguson, Brown and Gygi laboratories, Arshad Desai, Pablo Lara-Gonzalez, Hao Chen and Jason Yi for their feedback. We thank Cathie Janssen for schematics. We thank Eric Griffis and Peng Guo for microscopy guidance. Our work is supported by NIH T32GM008570 (DLB); NIH T32GM135095 (KAW); NIH R35GM128855 and UCRF (NGB); NIH GM67945 (SPG); and NIH 1K08HD099314 (CJF).

REFERENCES

1. Dikic I. (2017). Proteasomal and autophagic degradation systems. Annu. Rev. Biochem 86, 193–224. [PubMed: 28460188]
2. Pohl C & Dikic I (2019). Cellular quality control by the ubiquitin-proteasome system and autophagy. Science. 366, 818–822. [PubMed: 31727826]
3. Deshaies RJ & Joazeiro CAP (2009). RING domain E3 ubiquitin ligases. Annu. Rev. Biochem 78, 399–434. [PubMed: 19489725]
4. Chiurazzi P & Pirozzi F (2016). Advances in understanding – genetic basis of intellectual disability. F1000Research 5, 599.
5. Buiting K, Williams C & Horsthemke B (2016). Angelman syndrome-insights into a rare neurogenetic disorder. Nat. Rev. Neurol 12, 584–593. [PubMed: 27615419]
6. Chang L, Zhang Z, Yang J, McLaughlin SH & Barford D (2014). Molecular architecture and mechanism of the anaphase-promoting complex. Nature 17, 13–17.
7. Peters J-M (2006). The anaphase promoting complex/cyclosome: a machine designed to destroy. Nat. Rev. Mol. Cell Biol 7, 644–56. [PubMed: 16896351]
8. Huang J & Bonni A (2016). A decade of the anaphase-promoting complex in the nervous system. Genes Dev. 30, 622–638. [PubMed: 26980187]
9. Ferguson CJ et al. (2022). APC7 mediates ubiquitin signaling in constitutive heterochromatin in the developing mammalian brain. Mol. Cell 82, 90–105. [PubMed: 34942119]
10. Manivannan SN et al. (2022). De novo FZR1 loss-of-function variants cause developmental and epileptic encephalopathies. Brain 145, 1684–1697. [PubMed: 34788397]
11. Ajeawung NF et al. (2019). Mutations in ANAPC1, Encoding a Scaffold Subunit of the Anaphase-Promoting Complex, Cause Rothmund-Thomson Syndrome Type 1. Am. J. Hum. Genet 105, 625–630. [PubMed: 31303264]
12. Brown NG et al. (2016). Dual RING E3 architectures regulate multiubiquitination and ubiquitin chain elongation by APC/C. Cell 165, 1440–1453. [PubMed: 27259151]
13. Watson ER, Brown NG, Peters JM, Stark H & Schulman BA (2018). Posing the APC/C E3 Ubiquitin Ligase to Orchestrate Cell Division. Trends Cell Biol. 29, 117–134. [PubMed: 30482618]
14. Sivakumar S & Gorbsky GJ (2015). Spatiotemporal regulation of the anaphase-promoting complex in mitosis. Nat. Rev. Mol. Cell Biol 16, 82–94. [PubMed: 25604195]
15. Consalez GG, Goldowitz D, Casoni F & Hawkes R (2021). Origins, Development, and Compartmentation of the Granule Cells of the Cerebellum. Front. Neural Circuits 14, 1–23.
16. Yamada T, Yang Y & Bonni A (2013). Spatial organization of ubiquitin ligase pathways orchestrates neuronal connectivity. Trends Neurosci. 36, 218–226. [PubMed: 23332798]
17. Yang Y, Kim AH & Bonni A (2010). The dynamic ubiquitin ligase duo: Cdh1-APC and Cdc20-APC regulate neuronal morphogenesis and connectivity. Curr. Opin. Neurobiol 20, 92–99. [PubMed: 20060286]
18. García-Higuera I et al. (2008). Genomic stability and tumour suppression by the APC/C cofactor Cdh1. Nat. Cell Biol 10, 802–811. [PubMed: 18552834]
19. Manchado E et al. (2010). Targeting Mitotic Exit Leads to Tumor Regression In Vivo: Modulation by Cdk1, Mastl, and the PP2A/B55α,δ Phosphatase. Cancer Cell 18, 641–654. [PubMed: 21156286]
20. Matei V. et al. (2005). Smaller inner ear sensory epithelia in Neurog1 null mice are related to earlier hair cell cycle exit. Dev. Dyn 234, 633–650. [PubMed: 16145671]

21. Navarrete-Perea J, Yu Q, Gygi SP & Paulo JA (2018). Streamlined Tandem Mass Tag (SL-TMT) Protocol: An Efficient Strategy for Quantitative (Phospho)proteome Profiling Using Tandem Mass Tag-Synchronous Precursor Selection-MS3. J. Proteome Res 17, 2226–2236. [PubMed: 29734811]
22. Paulo JA et al. (2016). Quantitative mass spectrometry-based multiplexing compares the abundance of 5000 S. cerevisiae proteins across 10 carbon sources. J. Proteomics 148, 85–93. [PubMed: 27432472]
23. Carmena M, Wheelock M, Funabiki H & Earnshaw WC (2012). The chromosomal passenger complex (CPC): From easy rider to the godfather of mitosis. Nat. Rev. Mol. Cell Biol 13, 789–803. [PubMed: 23175282]
24. Jeyaprakash AA et al. (2007). Structure of a Survivin–Borealin-INCENP Core Complex Reveals How Chromosomal Passengers Travel Together. Cell 131, 271–285. [PubMed: 17956729]
25. Taggart JC, Zauber H, Selbach M, Li G-W & McShane E (2020). Perspective Keeping the Proportions of Protein Complex Components in Check. Cell Syst. 10, 125–132. [PubMed: 32105631]
26. Stewart S & Fang G (2005). Destruction box-dependent degradation of Aurora B is mediated by the anaphase-promoting complex/cyclosome and Cdh1. Cancer Res. 65, 8730–8735. [PubMed: 16204042]
27. Jarvis MA et al. (2016). Measuring APC/C-Dependent Ubiquitylation In Vitro. Methods Mol. Biol 1342, 287–303. [PubMed: 26254932]
28. Davey NE & Morgan DO (2016). Building a Regulatory Network with Short Linear Sequence Motifs: Lessons from the Degrons of the Anaphase-Promoting Complex. Mol. Cell 64, 12–23. [PubMed: 27716480]
29. Jumper J. et al. (2021). Highly accurate protein structure prediction with AlphaFold. Nature 596, 583–589. [PubMed: 34265844]
30. de la Torre-Ubieta L & Bonni A (2011). Transcriptional Regulation of Neuronal Polarity and Morphogenesis in the Mammalian Brain. Neuron 72, 22–40. [PubMed: 21982366]
31. Sillitoe RV, Lackey EP & Heck DH (2018). Recent advances in understanding the mechanisms of cerebellar granule cell development and function and their contribution to behavior. F1000Research 7, 1–12.
32. Bilimoria PM & Bonni A (2008). Cultures of cerebellar granule neurons. Cold Spring Harb. Protoc 3, 1–8.
33. Ostromyshenskii DI, Chernyaeva EN, Kuznetsova IS & Podgornaya OI (2018). Mouse chromocenters DNA content: Sequencing and in silico analysis. BMC Genomics 19, 1–15. [PubMed: 29291715]
34. Linhoff MW, Garg SK & Mandel G (2015). A High-Resolution Imaging Approach to Investigate Chromatin Architecture in Complex Tissues. Cell 163, 246–255. [PubMed: 26406379]
35. Hall LE, Mitchell SE & O'Neill RJ (2012). Pericentric and centromeric transcription: A perfect balance required. Chromosom. Res 20, 535–546.
36. Sobecki M. et al. (2016). The cell proliferation antigen Ki-67 organises heterochromatin. Elite 5, e13722.
37. Doench JG et al. (2016). Optimized sgRNA design to maximize activity and minimize off-target effects of CRISPR-Cas9. Nat. Biotechnol 34, 184–191. [PubMed: 26780180]
38. Scott SJ, Suvarna KS & D'Avino PP (2020). Synchronization of human retinal pigment epithelial-1 cells in mitosis. J. Cell Sci 133, 1–7.
39. Pérez-Cadahía B, Drobic B & Davie JR (2009). H3 phosphorylation: Dual role in mitosis and interphase. Biochem. Cell Biol 87, 695–709. [PubMed: 19898522]
40. Kill Ian R.. (1996). Localisation of the Ki-67 antigen within the nucleolus. Evidence for a fibrillarin-deficient region of the dense fibrillar component. J. Cell Sci 109, 1253–1263. [PubMed: 8799815]
41. Booth DG (2014). Ki-67 is a PP1-interacting protein that organises the mitotic chromosome periphery. Elite 3, e01641.
42. Padeken J & Heun P (2014). Nucleolus and nuclear periphery: Velcro for heterochromatin. Curr. Opin. Cell Biol 28, 54–60. [PubMed: 24690547]

43. Olsen JV et al. (2010). Quantitative phosphoproteomics revealswidespread full phosphorylation site occupancy during mitosis. Sci. Signal 3, 1–16.
44. Dephoure N. et al. (2008). A quantitative atlas of mitotic phosphorylation. Proc. Natl. Acad. Sci. U. S. A 105, 10762–10767. [PubMed: 18669648]
45. Nousiainen M, Silljé HHW, Sauer G, Nigg EA & Körner R (2006). Phosphoproteome analysis of the human mitotic spindle. Proc. Natl. Acad. Sci. U. S. A 103, 5391–5396. [PubMed: 16565220]
46. Kollareddy M. et al. (2012). Aurora kinase inhibitors: Progress towards the clinic. Invest New Drugs 30, 2411–2432. [PubMed: 22350019]
47. Komar D & Juszczynski P (2020). Rebelled epigenome: histone H3S10 phosphorylation and H3S10 kinases in cancer biology and therapy. Clin. Epigenetics 12, 1–14.
48. Borah NA & Reddy MM (2021). Aurora Kinase B Inhibition : A Potential Therapeutic Strategy for Cancer. Molecules 26, 1–30.
49. Lowenberg B. et al. (2011). Phase 1/2 study to assess the safety, efficacy, and pharmacokinetics of barasertib (AZD1152) in patients with advanced acute myeloid leukemia. Blood 118, 6030–6036. [PubMed: 21976672]
50. Schwartz GK et al. (2013). Phase I study of barasertib (AZD1152), a selective inhibitor of Aurora B kinase, in patients with advanced solid tumors. Invest New Drugs 2, 370–380.
51. Diaz RJ et al. (2015). Mechanism of action and therapeutic efficacy of Aurora kinase B inhibition in MYC overexpressing medulloblastoma. Oncotarget 6, 3359–3374. [PubMed: 25739120]
52. Crosio C. et al. (2002). Mitotic Phosphorylation of Histone H3 : Spatio-Temporal Regulation by Mammalian Aurora Kinases Mitotic Phosphorylation of Histone H3 : Spatio-Temporal Regulation by Mammalian Aurora Kinases. Mol. Cell. Biol 22, 874–885. [PubMed: 11784863]
53. Avagliano L. et al. (2020). Chromatinopathies: A focus on Cornelia de Lange syndrome. Clin. Genet 97, 3–11. [PubMed: 31721174]
54. Dunham I. et al. (2012). An integrated encyclopedia of DNA elements in the human genome. Nature 489, 57–74. [PubMed: 22955616]
55. Chen CCL et al. (2018). H3S10ph broadly marks early-replicating domains in interphase ESCs and shows reciprocal antagonism with H3K9me2. Genome Res. 28, 37–51. [PubMed: 29229671]
56. Politz JCR, Scalzo D & Groudine M (2016). The redundancy of the mammalian heterochromatic compartment. Curr. Opin. Genet. Dev 37, 1–8. [PubMed: 26706451]
57. Larson AG & Narlikar GJ (2018). The Role of Phase Separation in Heterochromatin Formation, Function, and Regulation. Biochemistry 57, 2540–2548. [PubMed: 29644850]
58. Dao TP et al. (2018). Ubiquitin Modulates Liquid-Liquid Phase Separation of UBQLN2 via Disruption of Multivalent Interactions. Mol. Cell 69, 965–978. [PubMed: 29526694]
59. Yasuda S. et al. (2020). Stress- and ubiquitylation-dependent phase separation of the proteasome. Nature 578, 296–300. [PubMed: 32025036]
60. Trivedi P & Stukenberg PT (2020). A Condensed View of the Chromosome Passenger Complex. Trends Cell Biol. 30, 676–687. [PubMed: 32684321]
61. Trivedi P. et al. (2019). The inner centromere is a biomolecular condensate scaffolded by the chromosomal passenger complex. Nat. Cell Biol 21, 1127–1137. [PubMed: 31481798]
62. Strom AR et al. (2017). Phase separation drives heterochromatin domain formation. Nature 547, 241–245. [PubMed: 28636597]
63. Larson AG et al. (2017). Liquid droplet formation by HP1α suggests a role for phase separation in heterochromatin. Nature 547, 236–240. [PubMed: 28636604]
64. Booth DG & Earnshaw WC (2017). Ki-67 and the Chromosome Periphery Compartment in Mitosis. Trends Cell Biol. 27, 906–916. [PubMed: 28838621]
65. Yamazaki H, Takagi M, Kosako H, Hirano T & Yoshimura SH (2022). Cell cycle-specific phase separation regulated by protein charge blockiness. Nat. Cell Biol 24, 625–632. [PubMed: 35513709]
66. Wiedner HJ & Giudice J (2021). It's not just a phase: function and characteristics of RNA-binding proteins in phase separation. Nat. Struct. Mol. Biol 28, 465–473. [PubMed: 34099940]
67. Guo Q, Shi X & Wang X (2021). RNA and liquid-liquid phase separation. Non-coding RNA Res. 6, 92–99.

68. Söding J, Zwicker D, Sohrabi-Jahromi S, Boehning M & Kirschbaum J (2019). Mechanisms for Active Regulation of Biomolecular Condensates. Trends Cell Biol. 30, 4–14. [PubMed: 31753533]
69. Leonard H, Petterson B, Bower C & Sanders R (2003). Prevalence of intellectual disability in Western Australia. Paediatr. Perinat. Epidemiol 17, 58–67. [PubMed: 12562473]
70. Boyle CA et al. (2011). Trends in the Prevalence of Developmental Disabilities in US Children, 1997-2008. Pediatrics 127, 1034–1042. [PubMed: 21606152]
71. Delgado-Esteban M, García-Higuera I, Maestre C, Moreno S & Almeida A (2013). APC/C-Cdh1 coordinates neurogenesis and cortical size during development. Nat. Commun 4, 2879. [PubMed: 24301314]
72. Meitinger F. et al. (2020). TRIM37 controls cancer-specific vulnerability to PLK4 inhibition. Nature 585, 440–446. [PubMed: 32908304]
73. Erickson BK et al. (2019). Active Instrument Engagement Combined with a Real-Time Database Search for Improved Performance of Sample Multiplexing Workflows. J. Proteome Res 18, 1299–1306. [PubMed: 30658528]
74. Schweppe DK et al. (2020). Full-featured, real-time database searching platform enables fast and accurate multiplexed quantitative proteomics. J. or Proteome Res 19, 2026–2034. [PubMed: 32126768]
75. McAlister GC et al. (2014). MultiNotch MS3 enables accurate, sensitive, and multiplexed detection of differential expression across cancer cell line proteomes. Anal. Chem 86, 7150–7158. [PubMed: 24927332]
76. Ting L, Rad R, Gygi SP & Haas W (2011). MS3 eliminates ratio distortion in isobaric multiplexed quantitative proteomics. Nat. Methods 8, 937–940. [PubMed: 21963607]
77. Tyanova S. et al. (2016). The Perseus computational platform for comprehensive analysis of (prote)omics data. Nat. Methods 13, 731–740. [PubMed: 27348712]
78. Eng JK, McCormack AL & Yates JRI (1994). An approach to correlate MS/MS data to amino acid sequences in a protein database. J. Am. Soc. Mass Spectrom 5, 976–989. [PubMed: 24226387]
79. Huttlin EL et al. (2010). A tissue-specific atlas of mouse protein phosphorylation and expression. Cell 143, 1174–1189. [PubMed: 21183079]
80. Gassaway BM et al. (2022). A multi-purpose, regenerable, proteome-scale, human phosphoserine resource for phosphoproteomics. Nat. Methods 19, 1371–1375. [PubMed: 36280721]
81. Perez-Riverol Y. et al. (2019). The PRIDE database and related tools and resources in 2019: Improving support for quantification data. Nucleic Acids Res. 47, D442–D450. [PubMed: 30395289]
82. Martinez-Chacin RC et al. (2020). Ubiquitin chain-elongating enzyme UBE2S activates the RING E3 ligase APC/C for substrate priming. Nat. Struct. Mol. Biol 27, 550–560. [PubMed: 32393902]
83. Qiao R, Weissmann F, Yamaguchi M, Brown NG, VanderLinden R, Imre R, Jarvis MA, Brunner MR, Davidson IF, Litos G, et al. (2016). Mechanism of APC/C-CDC20 activation by mitotic phosphorylation. PNAS 113, E2570–E2578. [PubMed: 27114510]
84. Schneider CA, Rasband WS & Eliceiri KW (2012). NIH Image to ImageJ: 25 years of image analysis. Nat. Methods 9, 671–675. [PubMed: 22930834]

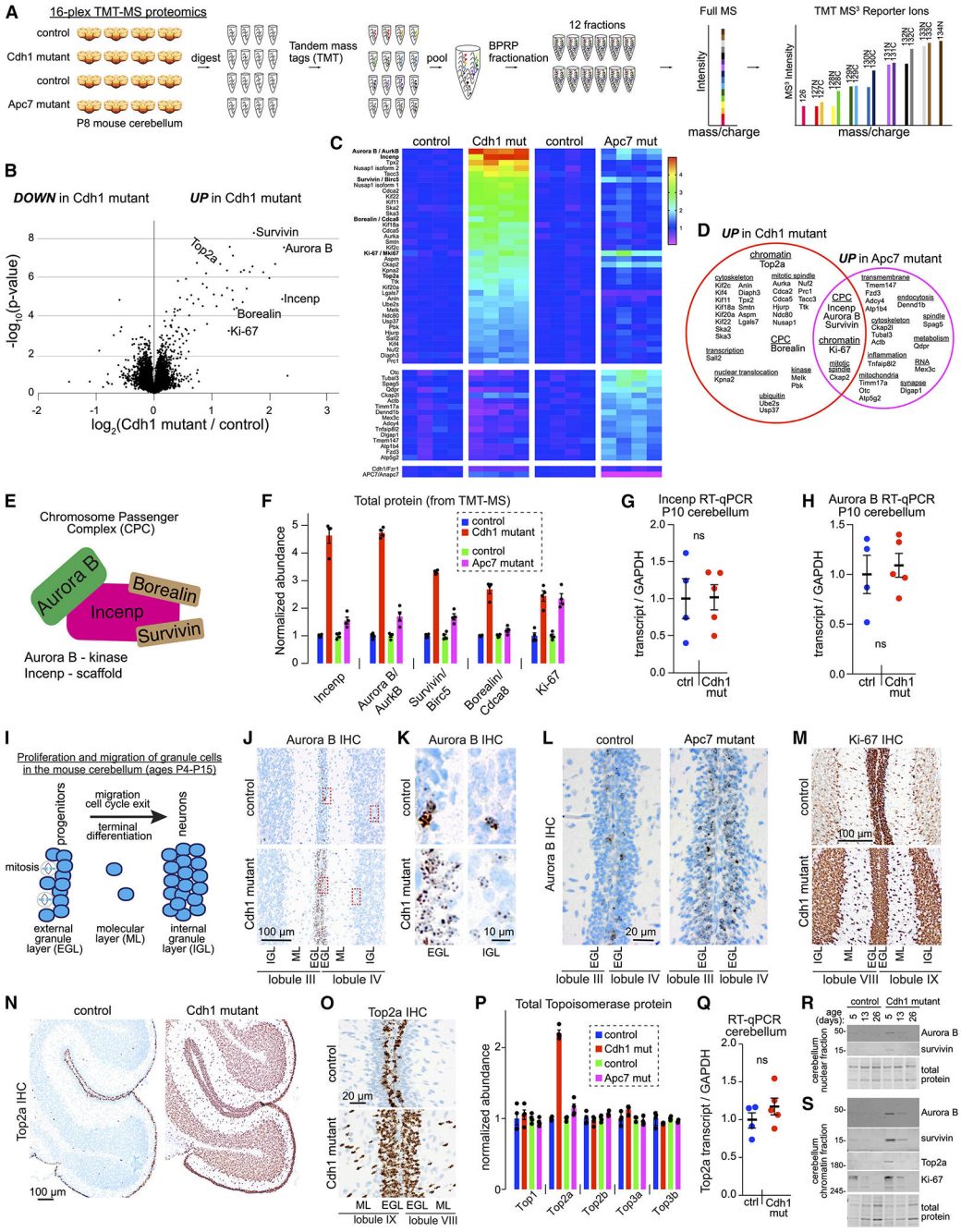

Figure 1: Proteomic identification of chromatin regulators as candidate APC substrates in the developing mouse cerebellum.

(A) Schematic of 16-plex Tandem Mass Tag (TMT) quantitative mass spectrometry (MS)-based proteomic evaluation of mouse cerebellum.

(B) Volcano plot of relative protein abundance in P8 Cdh1 mutant cerebellum.

(C) Heatmap showing the relative abundance of dysregulated proteins in Cdh1 and Apc7 mutant cerebellum. Significant hits were increased by >50% with p-value <0.01 by unpaired two-tailed t-test.

(D) Venn diagram of dysregulated proteins in Cdh1 and Apc7 mutant cerebellum.

(E) Subunits of the Chromosome Passenger Complex (CPC).
(F) Normalized abundance of the CPC and Ki-67 in the Apc7 and Cdh1 mutant cerebellum. Data from TMT-MS proteomics. Error bars, SEM.
(G) RT-qPCR analysis of Incenp normalized to GAPDH in nuclear RNA isolated from P10 mouse cerebellum. Error bars, SEM (n = 4 control, n = 5 Cdh1 mutant). Not significant by unpaired two-tailed t-test.
(H) RT-qPCR analysis of Aurora B. Error bars, SEM (n = 4 control, n = 5 Cdh1 mutant). Not significant by unpaired two-tailed t-test.
(I) Post-mitotic migration of cerebellar granule neurons.
(J) Immunohistochemistry (IHC) detection of Aurora B in the cerebellum of P10 mice.
(K) Higher magnification of Aurora B IHC.
(L) Aurora B IHC in P8 cerebellum.
(M) Ki-67 IHC in P10 cerebellum.
(N) Top2a IHC in P10 cerebellum.
(O) Top2a IHC in the EGL at P10.
(P) TMT-MS data for Topoisomerase enzymes in mouse cerebellum. Error bars, SEM.
(Q) RT-qPCR analysis of Top2a in nuclear RNA isolated from P10 mouse cerebellum. Error bars, SEM (n = 4 control, n = 5 Cdh1 mutant). Not significant by unpaired two-tailed t-test.
(R) Immunoblot (IB) of nuclear lysates isolated from the cerebellum at different ages.
(S) IB of cerebellar chromatin fraction at different ages.

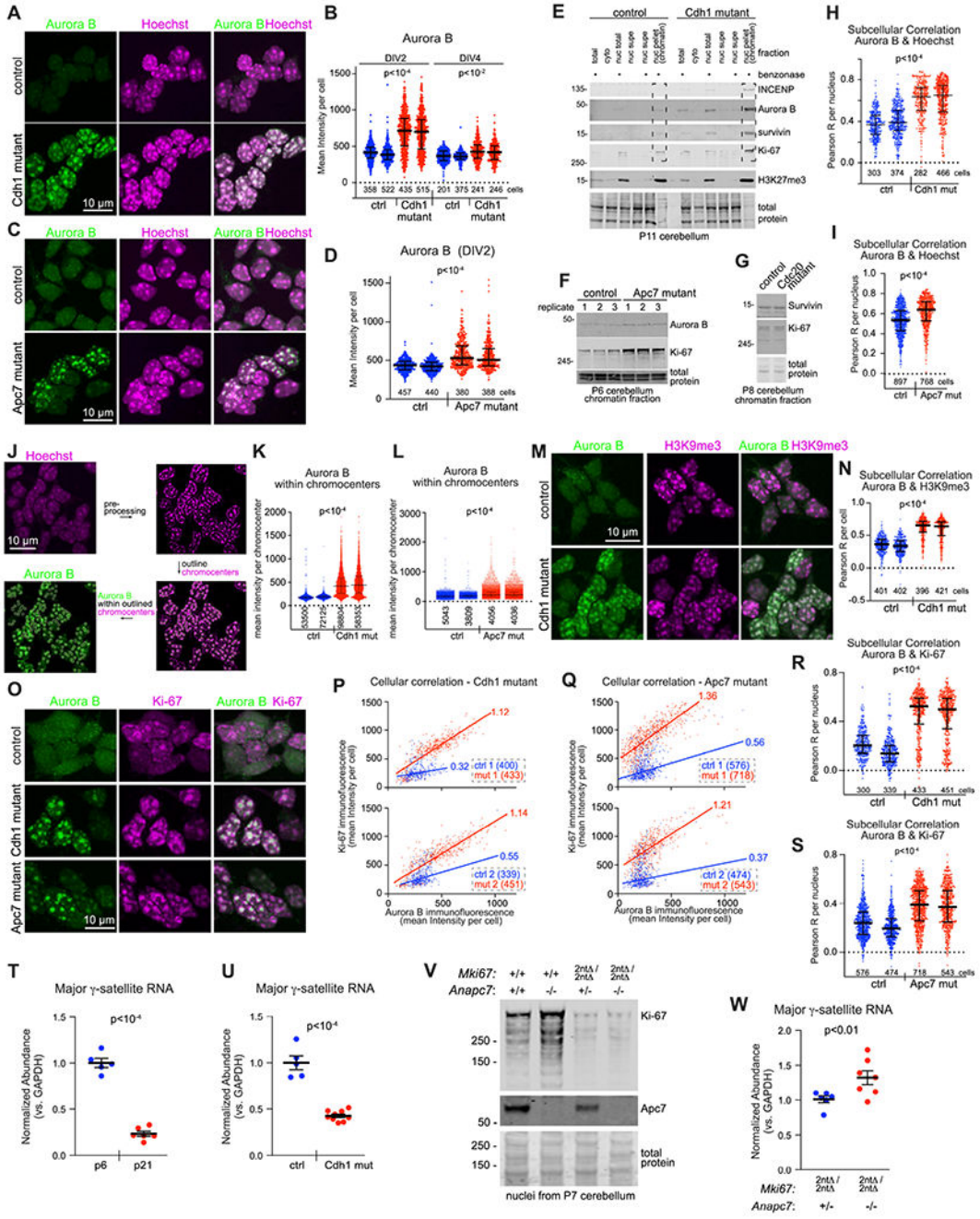

Figure 2: Aurora B accumulates in association with Ki-67 in APC mutant neurons and Ki-67 controls heterochromatin function.

(A) Immunofluorescence (IF) detection of Aurora B and confocal microscopy of primary mouse cerebellar granule neuron cultures at day 2 in vitro (DIV2).

(B) Quantitation of the mean fluorescence intensity for Aurora B on the indicated DIV. Error bars, interquartile range (IQR) (p-values by Kruskal-Wallis [K-W] test with Dunn test).

(C) IF detection of Aurora B and Hoechst in Apc7 mutant cultured cerebellar granule neurons (CGN).

(D) Quantitation of Aurora B intensity in Apc7 mutant CGN on DIV2 (number of cells shown). Error bars, IQR (p-values by K-W test with Dunn test).
(E) IB of CPC components and Ki-67 in biochemical fractions of mouse cerebellum. The endonuclease Benzonase digests chromatin. H3K27me3 is a modified histone protein. Total protein stained with the Revert reagent.
(F) IB of chromatin from Apc7 mutant cerebellum.
(G) IB of chromatin from Cdc20 mutant cerebellum.
(H) Subcellular correlation between Aurora B and Hoechst in Cdh1 mutant CGN on DIV2. The pixel-by-pixel Pearson correlation coefficient (R) was calculated within individual nuclei. Error bars, IQR (p-values by K-W test with Dunn test).
(I) Subcellular correlation between Aurora B and Hoechst in Apc7 mutant CGN on DIV2. Error bars, IQR (p-values by K-W test with Dunn test).
(J) Isolation of Hoechst-labeled chromocenters in confocal micrographs.
(K) Aurora B intensity within chromocenters of Cdh1 mutant CGN on DIV2 (number of chromocenters shown). Error bars, IQR (p-values by K-W test with Dunn test).
(L) Aurora B intensity within chromocenters of Apc7 mutant CGN on DIV2. Error bars, IQR (p-values by K-W test with Dunn test).
(M) IF Aurora B and H3K9me3 on DIV2.
(N) Subcellular correlation of Aurora B and H3K9me3 in DIV2 neurons. Error bars, IQR (p-values by K-W test with Dunn test).
(O) IF detection of Aurora B and Ki-67 in CGN on DIV2.
(P) Quantitation of cellular correlation by plotting the mean intensity of Ki-67 versus Aurora B in DIV2 CGN. Each data point represents a cell. Linear fit by robust regression, values indicate slope.
(Q) Cellular correlation of Ki-67 versus Aurora B in Apc7 mutant CGN on DIV2. Linear fit by robust regression.
(R) Subcellular correlation of Aurora B and Ki-67 in Cdh1 mutant CGN. Error bars, IQR (p-values by K-W test with Dunn test).
(S) Subcellular correlation of Aurora B and Ki-67 in Apc 7 mutant CGN. Error bars, IQR (p-values by K-W test with Dunn test).
(T) RT-qPCR detection of the major γ-satellite repeat RNA in mouse cerebellum. Total cerebellar RNA was treated with DNAse prior to cDNA synthesis, RT-qPCR and normalization to GAPDH. Error bars, SEM (p-values by Kolmogorov–Smirnov [K-S] test).
(U) RT-qPCR detection of the major γ-satellite RNA in nuclear RNA isolated from P10 mouse cerebellum. Error bars, SEM (p-values by K-S test).
(V) IB analysis of Ki-67 and Apc7 in nuclear lysates from P7 mouse cerebellum.
(W) RT-qPCR detection of the major γ-satellite repeat RNA in mouse cerebellum. *Mki67* encodes Ki-67. Error bars, SEM (p-values by K-S test).

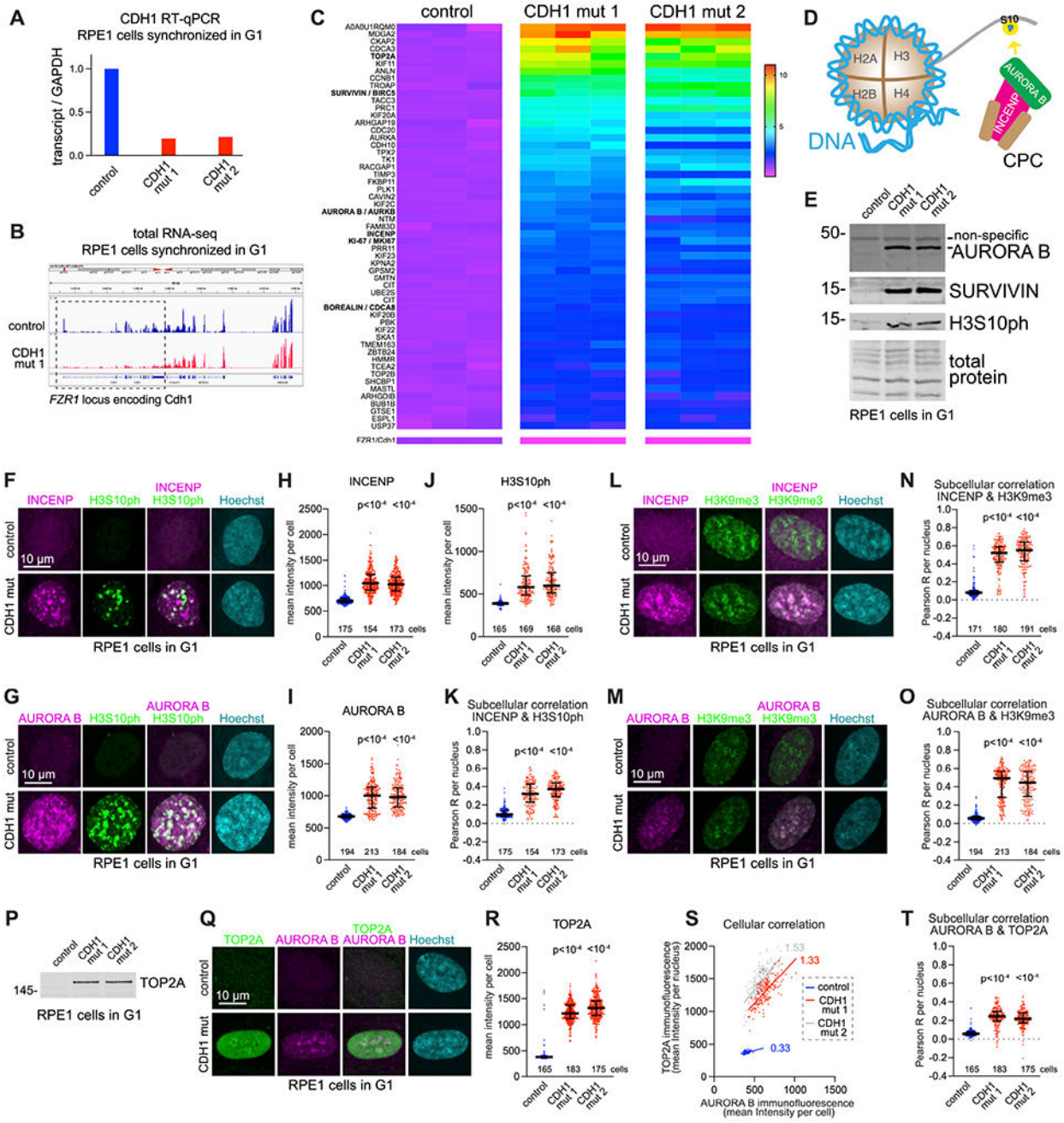

Figure 3: Elevation of neuronal APC substrates in G1-synchronized CDH1 mutant human RPE1 cells.

(T) CDH1 mutant cell lines were generated using two different guide RNAs (gRNAs) targeting *FZR1* in RPE1 cells expressing doxycycline-inducible Cas9. Stable lines were derived from isolated clones. Cells were synchronized in G1 by overnight application of 1 µM Palbociclib.

(A) CDH1 expression detected by RT-qPCR and normalized to GAPDH.

(B) RNA-seq analysis of the *FZR1* locus.

(C) TMT-MS proteomic analysis CDH1 mutant RPE1 cells. Heatmap depicts the normalized relative abundance of dysregulated proteins. Significantly elevated proteins were increased by >50% with p-value <0.01 by unpaired two-tailed t-test.
(D) Schematic diagram showing the enzymatic activity of the CPC kinase AURORA B and its product H3S10ph (histone 3 phosphorylated at Ser10).
(E) IB analysis of CPC components and H3S10ph.
(F) IF detection of INCENP and H3S10ph.
(G) IF detection of KI-67 and H3S10ph.
(H) INCENP fluorescence intensity. Error bars, IQR (p-values by K-W test with Dunn test).
(I) KI-67 fluorescence intensity. Error bars, IQR (p-values by K-W test with Dunn test).
(J) H3S10ph fluorescence intensity. Error bars, IQR (p-values by K-W test with Dunn test).
(K) Subcellular correlation of INCENP and H3S10ph. Error bars, IQR (p-values by K-W test with Dunn test).
(L) IF detection of INCENP and H3K9me3.
(M) IF detection of KI-67 and H3K9me3.
(N) Subcellular correlation of INCENP and H3K9me3. Error bars, IQR (p-values by K-W test with Dunn test).
(O) Subcellular correlation of KI-67 and H3K9me3. Error bars, IQR (p-values by K-W test with Dunn test).
(P) IB of TOP2A.
(Q) IF detection of TOP2A and KI-67.
(R) TOP2A fluorescence intensity. Error bars, IQR (p-values by K-W test with Dunn test).
(S) Cellular correlation of TOP2A versus KI-67. Linear fit by robust regression.
(T) Subcellular correlation of TOP2A and KI-67. Error bars, IQR (p-values by K-W test with Dunn test).

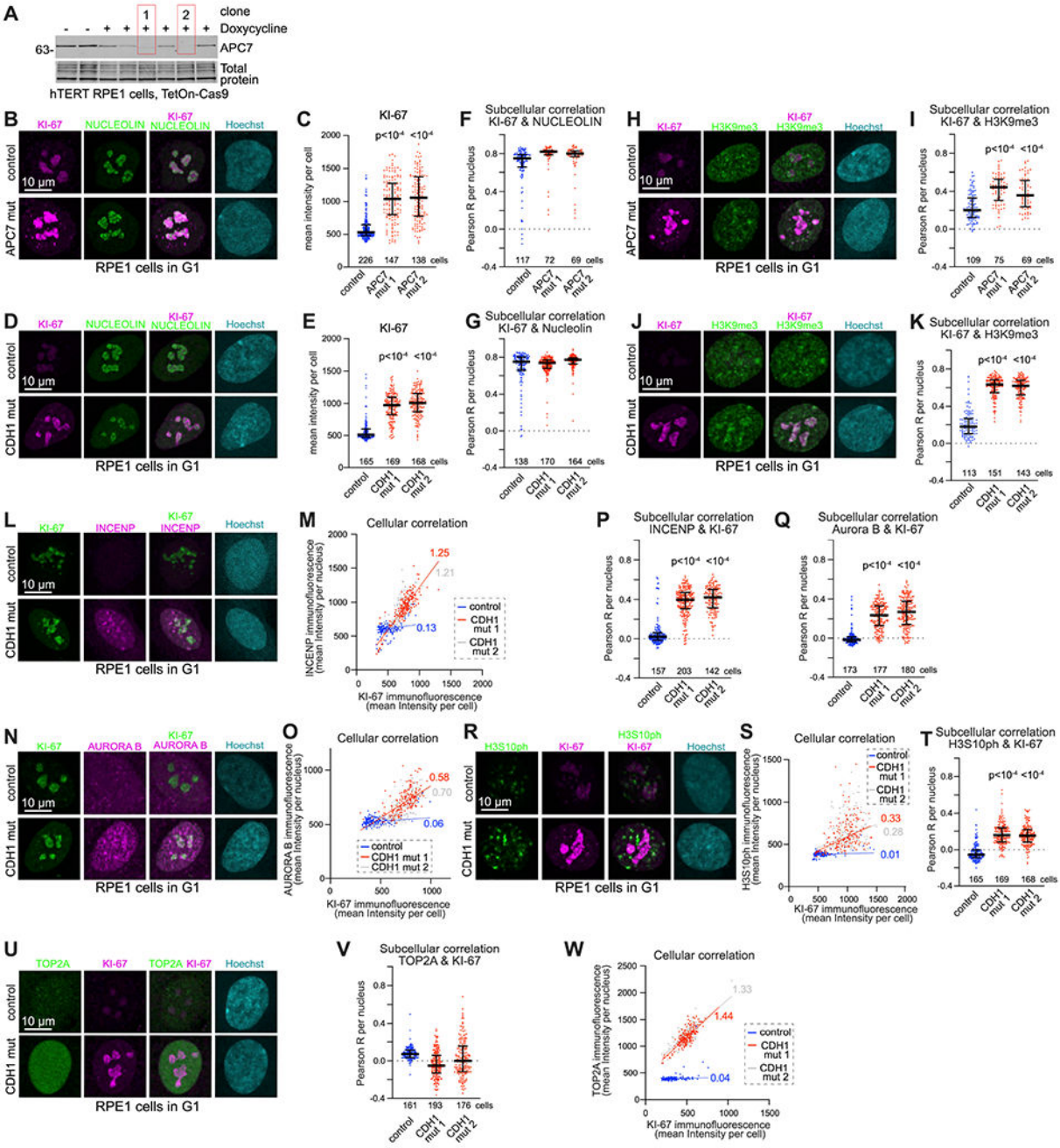

Figure 4: KI-67 accumulates within nucleoli and constitutive heterochromatin of APC mutant RPE1 cells.

(A) IB of APC7 in mutant RPE1 cell clones. Stable lines were derived from isolated clones after CRISPR targeting of *ANAPC7*.

(B) IF detection of KI-67 and NUCLEOLIN.

(C) KI-67 fluorescence intensity. Error bars, IQR (p-values by K-W test with Dunn test).

(D) IF detection of KI-67 and NUCLEOLIN.

(E) KI-67 fluorescence intensity. Error bars, IQR (p-values by K-W test with Dunn test).

(F) Subcellular correlation of KI-67 and NUCLEOLIN. Error bars, IQR (p-values by K-W test with Dunn test).
(G) Subcellular correlation of KI-67 and NUCLEOLIN. Error bars, IQR (p-values by K-W test with Dunn test).
(H) IF detection of KI-67 and H3K9me3.
(I) Subcellular correlation of KI-67 and H3K9me3. Error bars, IQR (p-values by K-W test with Dunn test).
(J) IF detection of KI-67 and H3K9me3.
(K) Subcellular correlation of KI-67 and H3K9me3. Error bars, IQR (p-values by K-W test with Dunn test).
(L) IF detection of INCENP and KI-67.
(M) Cellular correlation of INCENP versus KI-67. Linear fit by robust regression.
(N) IF detection of AURORA B and KI-67.
(O) Cellular correlation of AURORA B versus KI-67. Linear fit by robust regression.
(P) Subcellular correlation of INCENP and KI-67. Error bars, IQR (p-values by K-W test with Dunn test).
(Q) Subcellular correlation of AURORA B and KI-67. Error bars, IQR (p-values by K-W test with Dunn test).
(R) IF detection of H3S10ph and KI-67.
(S) Cellular correlation of H3S10ph intensity versus KI-67. Linear fit by robust regression.
(T) Subcellular correlation of H3S10ph and KI-67. Error bars, IQR (p-values by K-W test with Dunn test).
(U) IF detection of TOP2A and KI-67.
(V) Subcellular correlation of TOP2A and KI-67. Error bars, IQR (p-values by K-W test with Dunn test).
(W) Cellular correlation of TOP2A intensity versus KI-67. Linear fit by robust regression.

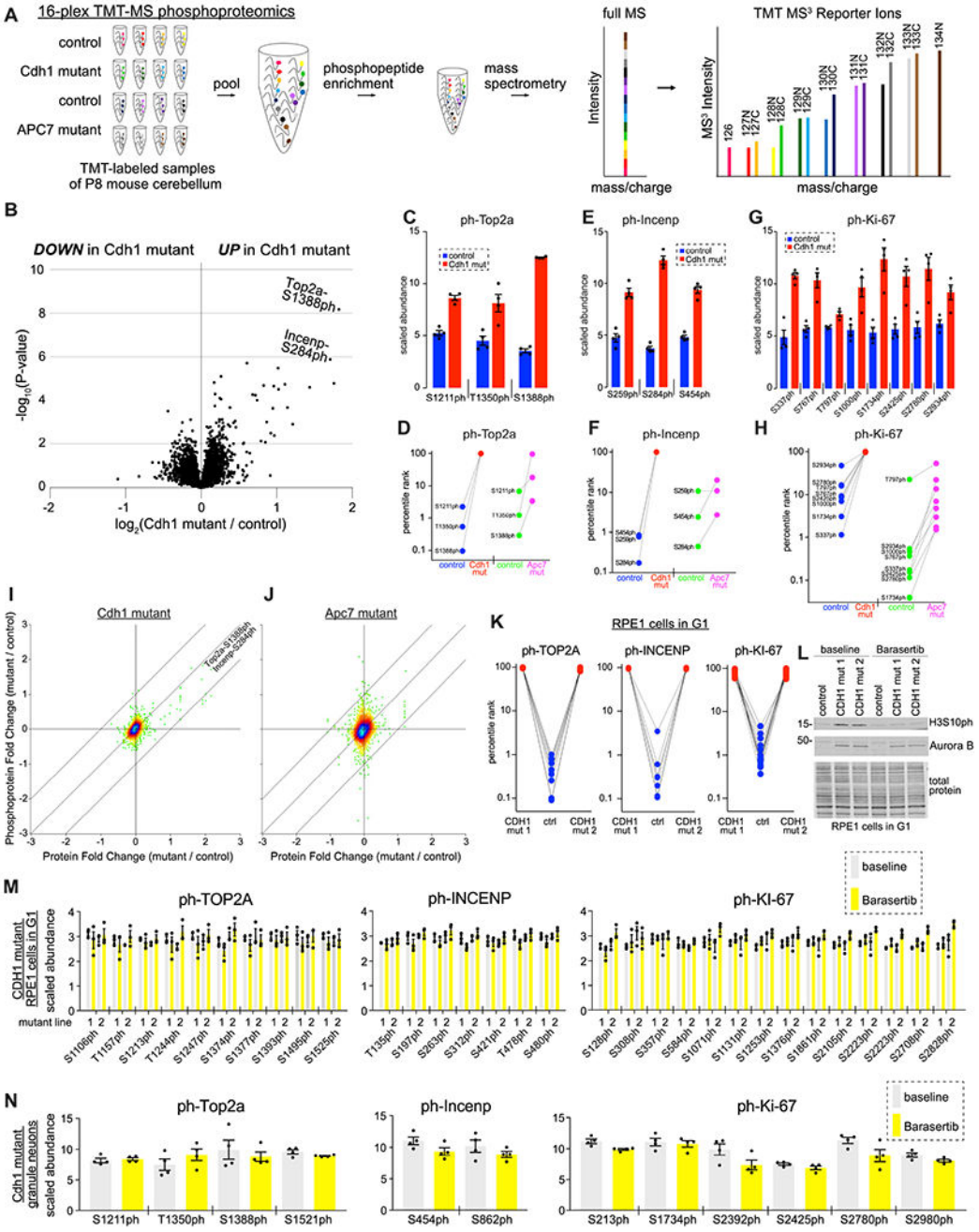

Figure 5: Phosphorylation of APC substrates is Aurora B independent.

(A) Schematic of 16-plex TMT-MS–based phosphoproteomic analysis of mouse cerebellum.

(B) Volcano plot showing the relative abundance of phosphoproteins in P8 mouse cerebellum.

(C) Scaled abundance of phosphorylation sites in ph-Top2a (phosphorylated Top2a) as quantified by TMT phosphoproteomics. Error bars, SEM.

(D) Percentile rank of phosphorylation sites in Top2a in control versus Cdh1 mutant. Phosphorylation sites were ordered by scaled abundance before determining their rank within the cerebellar phosphoproteome of each genotype.
(E) Scaled abundance of phosphorylation sites in ph-Incenp as quantified by TMT phosphoproteomics. Error bars, SEM.
(F) Percentile rank of phosphorylation sites in ph-Incenp.
(G) Scaled abundance of phosphorylation sites in ph-Ki-67 as quantified by TMT phosphoproteomics. Error bars, SEM.
(H) Percentile rank of phosphorylation sites in ph-Ki-67.
(I) Scatter plot showing the change in phosphoproteins versus the underlying proteins in the cerebellum. The x-axis shows the fold change of each underlying protein (Cdh1 mutant/control). The y-axis shows the fold change for each phosphorylation site (Cdh1 mutant/control).
(J) Scatter plot showing the change in phosphoproteins versus the underlying proteins in the Apc7 mutant cerebellum.
(K) Percentile rank of scaled abundance of ph-TOP2A, ph-INCENP and ph-KI-67 within the phosphoproteome of G1-synchronized Cdh1 mutant RPE1 cells. Multiplexed TMT-MS phosphoproteomic analysis was performed on 3 replicates from each lines. Phosphorylation sites were ordered by scaled abundance.
(L) IB of H3S10ph in RPE1 cells under baseline conditions versus Barasertib treatment. Synchronized RPE1 cells were treated with 1 μM Barasertib for 2 hours prior to cell lysis.
(M) TMT-MS phosphoproteomic analysis showing scaled abundance of phosphorylation sites in RPE1 cells under baseline conditions versus Barasertib treatment. Synchronized cells were treated with 1 μM Barasertib for 4 hours prior to lysis. Error bars, SEM.
(N) TMT-MS phosphoproteomic analysis showing scaled abundance of phosphorylation sites in DIV2 mouse CGN under baseline conditions versus Barasertib treatment. Error bars, SEM.

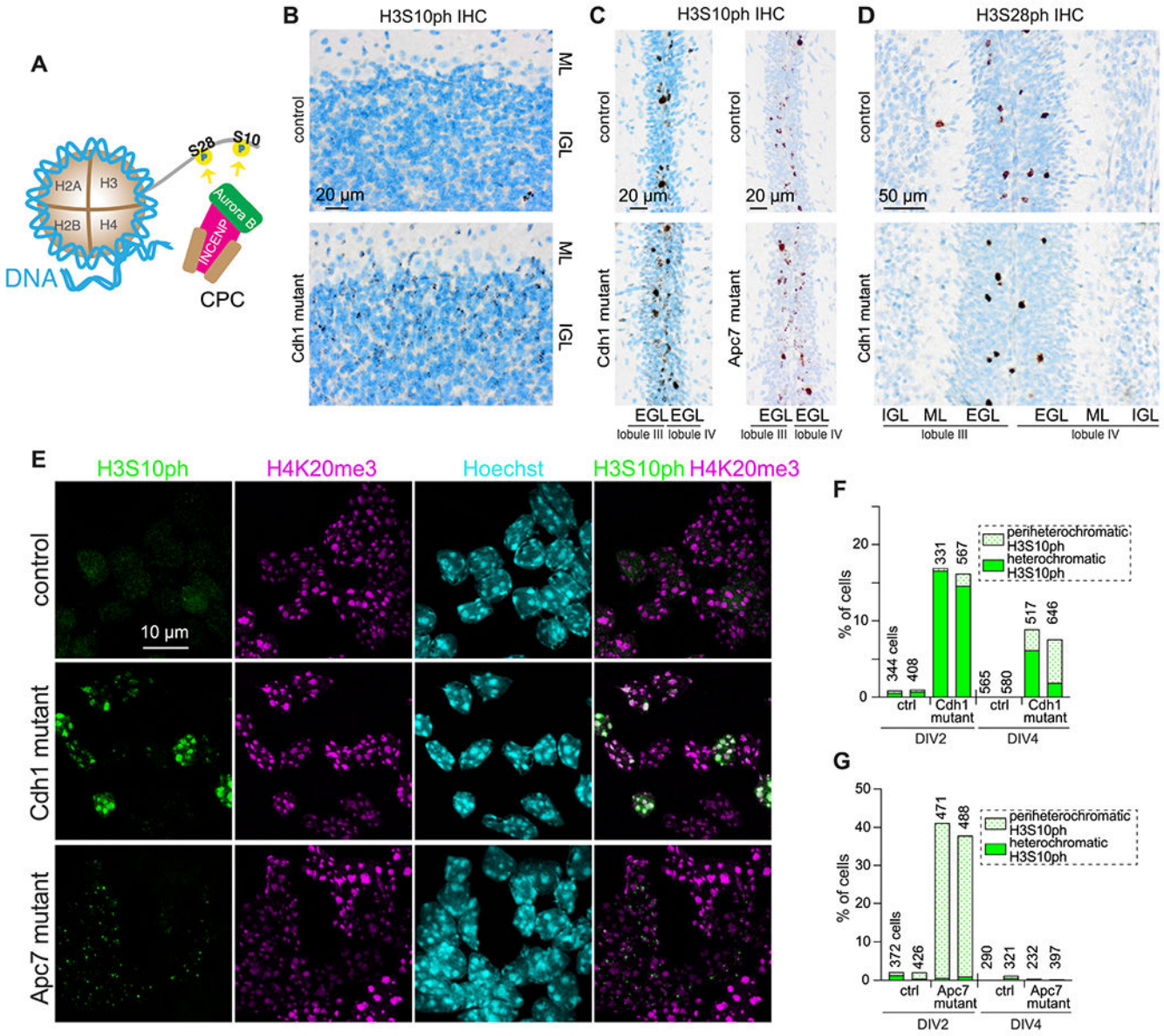

Figure 6: Histone 3 is hyperphosphorylated in post-mitotic APC mutant neurons.

(A) Schematic depiction of the CPC kinase Aurora B and its products H3S10ph and H3S28ph.

(B) IHC detection of H3S10ph in P10 mouse cerebellum.

(C) IHC of H3S10ph in the EGL of Cdh1 and Apc7 mutants.

(D) IHC of H3S28ph in P10 mouse cerebellum.

(E) IF detection of H3S10ph and H4K20me3, a modification associated with constitutive heterochromatin, in DIV2 CGN.

(F) Fraction of Cdh1 mutant CGN containing H3S10ph foci in a heterochromatic versus perheterochromatic pattern.

(G) Analysis of the pattern of H3S10ph foci in Apc7 mutant CGN.

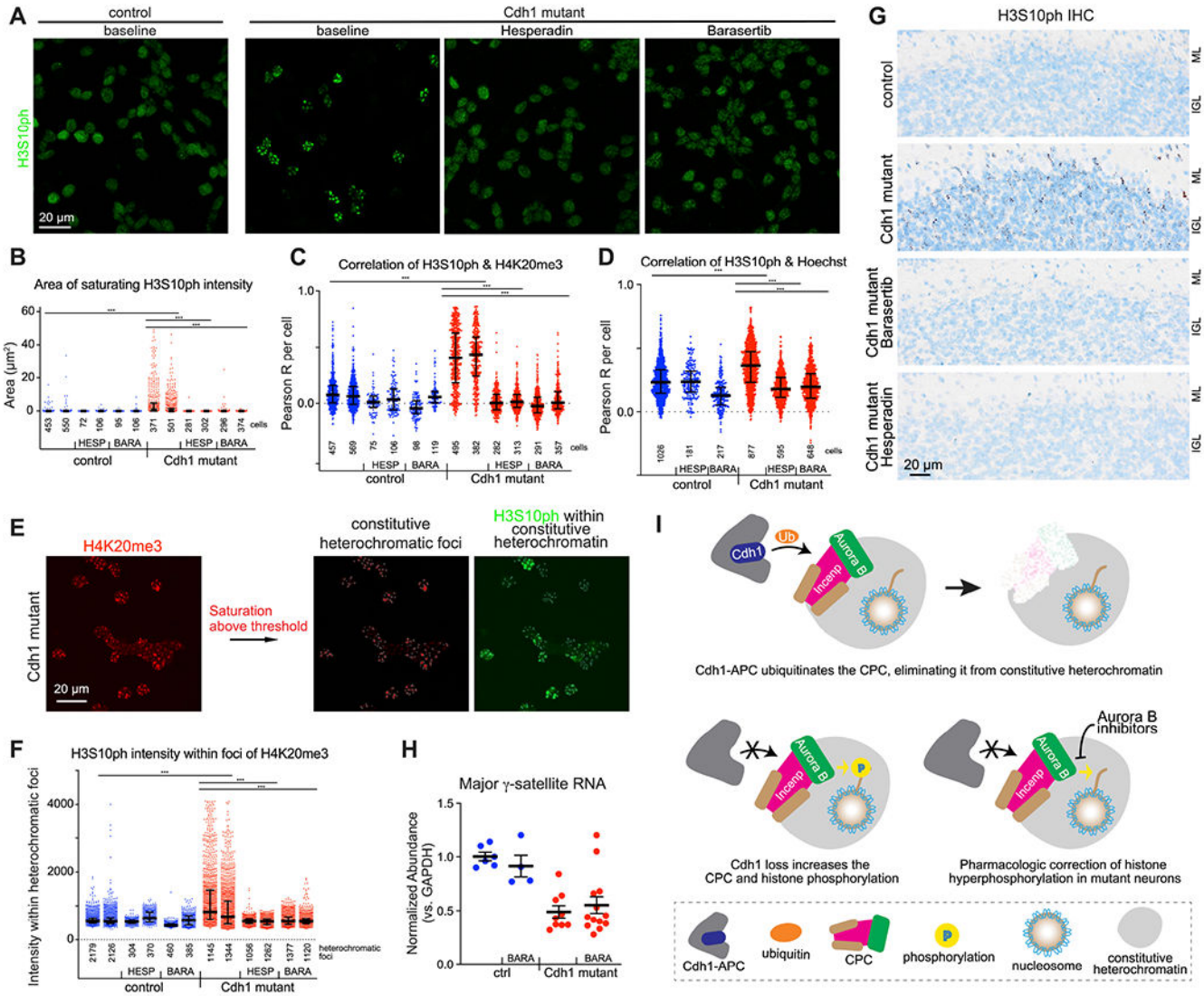

Figure 7: Aurora B inhibitors partially rescue chromatin dysregulation in APC mutant neurons.

(A) IF detection of H3S10ph in DIV2 Cdh1 mutant CGN under baseline conditions versus 2 hour treatment with 0.5 μM Hesperadin or 1 μM Barasertib.

(B) Saturating area of H3S10ph signal in nuclei under baseline conditions versus drug treatment. Error bars, IQR (p-values by K-W test with Dunn test). *** indicates p-value $<10^{-4}$.

(C) Subcellular correlation of H3S10ph and H4K20me3 in DIV2 CGN under baseline conditions versus drug treated. Error bars, IQR (p-values by K-W test with Dunn test). *** indicates p-value $<10^{-4}$.

(D) Subcellular correlation of H3S10ph and Hoechst in DIV2 CGN. Error bars, IQR (p-values by K-W test with Dunn test). *** indicates p-value $<10^{-4}$.

(E) Isolation of H4K20me3-labeled constitutive heterochromatic foci in confocal photomicrographs.

(F) H3S10ph fluorescence intensity within heterochromatic foci. Error bars, IQR (p-values by K-W test with Dunn test)

(G) H3S10ph IHC in the Cdh1 mutant cerebellum. P10 mice received subcutaneously injections of either 5 mg/kg Hesperadin or 25 mg/kg Barasertib 4 hours before tissue collection.

(H) RT-qPCR detection of the major γ-satellite RNA in mouse cerebellum. Treated mice received 30 mg/kg Barasertib daily from P8 to P11 before collecting tissue 4 hours later on P11.

(I) Schematic depiction showing the regulation of H3S10ph by Cdh1-APC and the potential therapeutic role for Aurora B inhibitors upon CPC dysregulation.

KEY RESOURCES TABLE

REAGENT or RESOURCE	SOURCE	IDENTIFIER
Antibodies		
Rabbit polyclonal anti-APC7 C-term	Bethyl	Cat# A302-551A, RRID:AB_1998911
Rabbit anti-APC1	Bethyl	Cat# A301-653A-T, RRID:AB_2632162
Mouse monoclonal (DH01) anti-FZR1/CDH1	Thermo Fisher Scientific	Cat# MA5-11496, RRID:AB_10979615
Rat monoclonal anti-Ki-67 (SolA15)	Thermo Fisher Scientific	Cat# 14-5698-82, RRID:AB_10854564
Purified Mouse anti-Aim1 / Aurora B (IF, IB)	BD Biosciences	Cat# 611082, RRID:AB_2227708
Rabbit monoclonal anti-Aurora B (IHC)	Abcam	Cat# ab287960, RRID: not found
Anti-H3S10ph (IF neurons)	Millipore	Cat# 06-570, RRID:AB_310177
Anti-H3S10ph (IHC)	Cell Signaling Technology	Cat# 9701, RRID: AB_331535
Rabbit polyclonal anti-H3S10ph (IF mitosis)	Active Motif	Cat# 39253, RRID:AB_2793206
Rabbit monoclonal anti-Survivin	Cell Signaling Technology	Cat# 71G4B7, RRID:AB_2063948
Rabbit monoclonal anti-Top2a	Abcam	Cat# ab52934, RRID:AB_883143
Rabbit anti-H3K9me3	Active Motif	Cat# 39286, RRID: AB_2935892
Rabbit monoclonal anti-H3K27me3	Cell Signaling Technology	Cat# 9733S, RRID:AB_2616029
Mouse anti-H4K20me3	Abcam	Cat# ab78517, RRID:AB_1951279
Rabbit anti-Incenp (IB)	Proteintech	Cat# 29419-1-AP, RRID:AB_2918303
Mouse anti-INCENP	Active Motif	Cat# 39259, RRID:AB_2715518
Rabbit polyclonal anti-H3K27ac	Active Motif	Cat# 39034, RRID:AB_2722569
Rabbit anti-HP1a	Cell Signaling Technology	Cat# 2616S, RRID:AB_2070987
Rabbit anti-nucleolin	Bethyl	Cat# IHC-00083, RRID:AB_2267070
Goat anti-Mouse IgG (H+L) Highly Cross-Adsorbed Secondary, Alexa Fluor 568	Thermo Fisher Scientific	Cat# A-11031, RRID:AB_144696
Goat anti-Rat IgG (H+L) Cross-Adsorbed Secondary, Alexa Fluor 488	Thermo Fisher Scientific	Cat# A-11006, RRID:AB_2534074
Goat anti-Rat IgG (H+L) Cross-Adsorbed Secondary, Alexa Fluor 568	Thermo Fisher Scientific	Cat# A-11007, RRID:AB_2896333
Donkey anti-Rabbit IgG (H+L) Highly Cross-Adsorbed Secondary, Alexa Fluor 488	Thermo Fisher Scientific	Cat# A-21206, RRID:AB_2535792
Donkey Anti-Mouse IgG IRDye 680 Conjugated antibody	LI-COR Biosciences	Cat# 926-32222, RRID:AB_621844
IRDye 800CW Donkey anti-Rabbit IgG antibody	LI-COR Biosciences	Cat# 925-32213, RRID:AB_2715510
IRDye 800CW Goat anti-Rat IgG antibody	LI-COR Biosciences	Cat# 926-32219, RRID:AB_1850025
AffiniPure Rabbit Anti-Rat IgG (H+L)	Jackson Immuno Research	Cat# 312-005-045, RRID:AB_2339803
OmniMap DAB anti-Rb	Ventana Medical systems	Cat# 05266548001, RRID: Not Found
Chemicals, Peptides, and Recombinant Proteins		
UBE1 (E1)	(Jarvis et al., 2016[27])	N/A
CDH1 protein	(Jarvis et al., 2016[27])	N/A
UBCH10 (E2)	(Jarvis et al., 2016[27])	N/A
UBE2S (E2)	(Jarvis et al., 2016[27])	N/A
Fluorescent cyclin B1-NTD (CycB-NTD)	(Jarvis et al., 2016[27])	N/A

REAGENT or RESOURCE	SOURCE	IDENTIFIER
ubiquitin	(Jarvis et al., 2016[27])	N/A
Ki-67 AA 1-300	(Ferguson et al., 2022[9])	N/A
Benzonase	Millipore	E1014
Doxycycline Hyclate, 98%	Thermo Scientific	AC446060050
Hoechst 33258 solution	Millipore Sigma	Cat# 94403
TMT11 reagent	Thermo Fisher Scientific	A37727
TMT16 reagent	Thermo Fisher Scientific	A44520
TMTpro	Thermo Fisher Scientific	A44520
Pierce Trypsin Protease, MS Grade	Thermo Fisher Scientific	Cat#90305
Acetonitrile	Honeywell	AS017-0100
Lys-C, Mass Spectrometry Grade	Wako Chemicals	129-02541
Palbociclib	Selleck Chemical LLC	50-854-7
Pierce Phosphatase Inhibitor Mini Tablets (TMT/MS)	Thermo Fisher Scientific	A32957
Pierce Protease Inhibitor Mini Tablets (TMT/MS)	Thermo Fisher Scientific	A32953
Protease inhibitor cocktail	Sigma	P8340
Phosphatase inhibitor cocktail #3	Sigma	P0044
PMSF	Sigma	PMSF-RO
Polybrene	EMD Millipore	TR-1003-G
Puromycin	Thermo Fisher Scientific	J67236.XF
PEG-it Virus Precipitation Solution	System Biosciences	LV810A-1
HyClone Fetal Bovine Serum	Cytiva	SH30071.03IH25-40
Pierce BCA Protein Assay	Thermo Fisher Scientific	Cat# 23223
Bradford regent	Bio-Rad	Cat# 5000006
Revert total protein stain	LI-COR	Cat# 926-11011
iScript cDNA synthesis kit	Bio-Rad	Cat# 1708890
Lenti-X TM Packaging Single Shots (VSV-G)	Takara Bio	Cat# 631275
Barasertib (AZD1152)	MedChemExpress	Cat# HY-10127
Hesperadin	Cayman Chemical	Cat# 24199
Deposited Data		
Investigation of cerebellum-specific knockouts of Cdh1 and Apc7	This Study (Table S2)	(http://www.ebi.ac.uk/pride) PXD038778
Phosphoproteomic analysis of Aurora B inhibition in WT and CDH1 mutant RPE1 cells	This Study (Table S3)	(http://www.ebi.ac.uk/pride) PXD044042
Investigating the effect of Aurora B inhibition in WT and Cdh1 mutant primary neuron cultures	This Study (Table S4)	(http://www.ebi.ac.uk/pride) PXD045116
Original/source data	Mendeley Data	DOI: 10.17632/5f5mhb8yzv.1
Experimental Models: cell lines		
RPE-1 CEP192-mNeonGreen TetOn-Cas9	(Meitinger et al., 2020[72])	ODCL0191
RPE-1 CEP192-mNeonGreen TetOn-Cas9 ANAPC7 gRNA #4	(Ferguson et al., 2022[9])	N/A
RPE-1 CEP192-mNeonGreen TetOn-Cas9 FZR1 gRNA #1	This study	N/A

REAGENT or RESOURCE	SOURCE	IDENTIFIER
RPE-1 CEP192-mNeonGreen TetOn-Cas9 FZR1 gRNA #2	This study	N/A
RPE-1 CEP192-mNeonGreen TetOn-Cas9 FZR1 gRNA #3	This study	N/A
RPE-1 CEP192-mNeonGreen TetOn-Cas9 FZR1 gRNA #4	This study	N/A
Experimental Models: Organisms/Strains		
Anapc7 mutant on hybrid C57BL/6 x 129	(Ferguson et al., 2022[9])	
Anapc7 mutant on Jackson C57BL/6	(Ferguson et al., 2022[9])	N/A
Cdc20$^{f/f}$ mice on C57BL/6	(Manchado et al., 2010[19])	N/A
Fzr1$^{f/f}$ mice on C57BL/6	(García-Higuera et al., 2008[18])	N/A
Math1/Atoh1-cre mice on C57BL/6	The Jackson Laboratory	Cat# 011104
Mki67 mutant on C57BL/6	(Sobecki et al., 2016[36])	N/A
Wild-type Jackson C57BL/6	The Jackson Laboratory	Cat# 000664
Oligonucleotides		
See Table S1		
Recombinant DNA/Cloning		
pGEX-INCENP amino acids 256-632	This study	N/A
pGEX-INCENP amino acids 256-563	This study	N/A
pGEX-INCENP amino acids 256-563, Δ493-496, Δ539-542	This study	N/A
NEB 5-alpha Competent E.Coli (High efficiency)	New England Biolabs	Cat# C2987H
Monarch Plasmid Miniprep kit	New England Biolabs	Cat# T1010S
BamHI- HF	New England Biolabs	Cat# R3136T
NotI-HF	New England Biolabs	Cat# R3189S
Esp3I	Thermo Scientific	Cat# FERER0451
Monarch PCR and DNA Cleanup Kit	New England Biolabs	Cat# T1030S
Monarch DNA Gel Extraction Kit	New England Biolabs	Cat# T1020S
Software and Algorithms		
AlphaFold	(Jumper et al., 2021[29])	https://alphafold.ebi.ac.uk
ImageJ	(Schneider et al., 2012[84])	https://imagej.nih.gov/ij/
NIS - Elements	Nikon	RRID:SCR_014329
Image Studio	LI-COR	N/A
ImageLab	Bio-rad	N/A
CFX Maestro	Bio-Rad	N/A
SEQUEST-based in-house platform	Thermo Fisher Scientific (Eng et al., 1994[78]; Huttlin et al., 2010[79])	http://fields.scripps.edu/yates/wp/?page_id=17
Other		
Ventana Discovery Ultra	Roche Diagnostics	RRID: SCR_021254
Rneasy Mini Kit	Qiagen	Cat# 74104
Sep-Pak cartridge	Waters	WAT054925
Fe-NTA spin column	Thermo Fisher	A32992